Università degli Studi di Ferrara

DOTTORATO DI RICERCA IN FISICA

CICLO XXVI

COORDINATORE Prof. Vincenzo Guidi

K-edge filter subtraction technique used for mapping elemental distribution on paintings

Settore Scientifico Disciplinare FIS/07

Dottorando

Dott. Irena Muçollari

Tutore

Prof. Mauro Gambaccini

Co -Tutore

Dr. Giovanni Di Domenico

Anni 2011/2013

Abstract

Several techniques exist for mapping the element pigments on painting using the synchrotron light or quasi monochromatic sources. K-edge subtraction technique is a well known technique and based on discontinuity in the attenuation coefficient due to photoelectric *K*-edge of the absorbing materials. A couple of filters with slightly different *K* -edge energies, if are with balanced thicknesses, can isolate spectra in a narrow energy band. Quasi monoenergetic X-rays with a spectral width ΔE_k that is the difference in *K*-edge energies will be taken by subtracting images or spectral data.

Thus by using filter foils with appropriate thicknesses with the *K*-edge absorption just below and above the *K*-edge energy of an element allows us evaluating the distribution of that element in whole painting.

The aim of this thesis has been application of *K*-edge subtraction technique to determine pigment composition in paintings by using common X-ray sources with balanced filters.

The *K*-edge digital subtraction technique actually is investigated for estimation of Cadmium element. By choosing the Silver Cadmium and Indium as filter materials with properly thickness and with *K*-edge energies very close to the Cadmium element, determination of cadmium content has been presented as qualitative and quantitative result. The technique is tested by using a RadEye200 CMOS sensor. Theoretical simulations considering the experimental setup of technique has been presented as preliminary investigation. Complementary analyses are preformed with micro X-ray fluorescence spectrometry (μXRF), in order to validate the technique for cadmium element with the same samples.

Theoretical aspects of K-edge imaging, the algorithms used for elaboration of images, detailed information for cadmium pigments and samples tests, are described in first chapters. An evaluation of X-ray performance of RadEye200 CMOS sensor has been performed in terms of MTF, NPS and DQE.

Preliminary theoretical simulation is performed to determine the range where KES imaging technique with balanced filters response linear with the element content in paintings.

In chapter 5 after description of spectral characteristics of the tungsten X-ray tube with additional K-edge filtering, imaging and steps of elaborating images has been described. Determination of Cadmium element in its pigments it is performed by KES and Lehmann algorithm applied on digital images. Results obtained on different samples are presented by a couple of images, graphically, tabulated data, and discussed.

In chapter 6 introduction in theoretical aspects of XRF spectrometry is presented. Measurements for sampling area of μXRF ArtaxBruker200 and for Cadmium content in same samples used for imaging are presented.

In chapter 7 the results carry out from KES technique and XRF for cadmium element in different samples are compared. The comparison between KES and XRF technique performed with the same sampling area of two detection systems (CMOS sensor with SDD solid drift detector) on the same area of the test sample shows a very good correlation among them.

Key words

X-ray, *K*-edge, KES, digital radiography, imaging, balanced filters, μXRF spectrometry, Cadmium pigments.

Acknowledgements

I would like to thank a number of people who have helped and encouraged me during the period of PhD research at the University of Ferrara. Firstly, I would like to express my personal gratitude to my supervisors, Prof. Mauro Gambaccini and Prof. Giovanni Di Domenico, for their continued support and advice during the course of this thesis.

Also I would like to express my gratitude to the all members of Medical Physics group at University of Ferrara, Angelo Taibi, Paolo Cardarelli, Gaia Pupillo, Michele Marziani, Francesco Sisini which have helped me in the beginning to enter in this new field and for their support and encouragement.

Many thanks to Prof. Petrucci, Flavia Tisato and Eva Peccenini. I really appreciate their willingness to help me in performing XRF measurements.

I would like to thank friends and colleagues that I have discussed with during this period especially Paolo, Gaia, Fausia, Manjola, Anahita and Ennam, for giving me so many assistance.

Moreover, I am highly thankful to many other kind people who became Cenacolist's friends for me. Thank you for sharing your experience about world, life, culture, people and kindness with me. You became my family here in Italy and I am so happy for having this chance to meet all of you in the same place.

Finally a special thank goes to my family for the persistent support, love and care and trust that they gave to me. I feel so lucky to have such a wonderful, devoted and loveable parents, siblings and family.

I would like to extend as well my thanks to those who indirectly contributed in this research, your kindness means a lot to me .

Ferrara, 27th February 2014

Contents

List of figures and tables

CHAPTER 1

CHAPTER 2

CHAPTER 3

CHAPTER 4

CHAPTER 7

Introduction

Several techniques exist for mapping the element pigments on painting using the synchrotron light or quasi monochromatic sources. The aim of this thesis has been in application of *K*-edge subtraction technique to determine pigment composition in paintings by using common X-ray sources with balanced filters.

K-edge filtration is a well known technique and based on discontinuity in the attenuation coefficient due to photoelectric *K*-edge of the absorbing materials. A couple of filters with slightly different k-edge energies, if are with balanced thicknesses, can isolate spectra in a narrow energy band. Quasi monoenergetic X-rays with a spectral width ΔE_k that is the difference in *K*-edge energies will be taken by subtracting images or spectral data [1][2][3]. Thus using filter foils with appropriate thicknesses with the *K*-edge absorption just below and above the *K*-edge energy of an element allow us evaluating the distribution of that element in whole paint.

Logarithmic subtraction of high- and low energy-images gives qualitative measurements but processing images with Lehmann algorithm gives information on the mass density of target element. Determination of cadmium element in its pigments it is performed by KES and Lehmann algorithm applied on digital images acquired.

The X-ray unit was the Tungsten tube filtered by a set of filters Silver Cadmium and Indium. Analytical simulations for foreseen signal produced on a CMOS RadEye200 digital detector are built to validate the technique.

Cadmium element in its pigments it is investigated in artificial phantoms and real paints

In additional with the same samples complementary analyses are preformed with micro X-ray fluorescence spectrometry (μXRF) and it is determined a linear correlation between results.

CHAPTER 1

1. K-edge Imaging

In this chapter a theoretical introduction of main topics of this work will be presented. Conventional techniques in mapping elemental distribution in paints are mentioned with their advantages and disadvantages. Main procedure for elaborating digital images and algorithms for quantitatively evaluations are presented analytically.

1.1 Introduction to elemental mapping techniques on paintings: KES technique

The X-transmission radiography plays an important role in the examination of paintings.
It provides information on execution techniques and under paintings based on X-ray attenuation by materials that compose the painting, however, does not provide elemental composition.

X-ray fluorescence spectrometry (XRF) and particle induced X-Ray emission (PIXE) are the main methods used for elemental composition of pigments in paintings. These techniques allow for detection of elements on a painting but their trade-off is the inspection is intrinsically local and takes a long time acquisitions.

The conventional *K*-edge subtraction technique it is used for tracing the contrast element in medicine [4] or elements with interest in mapping paintings [5][6] using the synchrotron light or quasi monochromatic sources.

This technique takes advantage of the sharp rise of X-ray absorption coefficient of the elements, the *K*-edge discontinuity. By using common X-ray tube three radiographies must be performed, including *k*-edge filters that bracket the edge energy of element of interest. Making the difference between adjacent *K*-edge filter images acquired by an integrator digital X-ray detector will be obtained the *Low* and *High* energy images which will present pseudo-monochromatic images. In this way, considering that *Low* and *High* energy image have information in narrow bin energy width (not more than 2keV) just below and above the edge energy of the element of interest means to have a high signal variation of target element and almost constant response from the background.

The images are processed by linear subtraction and Lehmann algorithm. Applying the linear subtraction on images qualitative information will be obtained in terms of distribution of element in digit numbers (gray level). Quantitative evaluation in terms of mass density distribution (g/cm^2) of the *K*-edge element will be obtained by Lehmann algorithm.

In this work it is investigated the KES technique in elemental mapping of paintings by using a conventional X-ray tube with balanced filters. The advantage is that inspection is not intrinsically local but *K*-edge imaging allows to map elements in large area and in a short time.

1.2 Attenuation of X-rays

X ray is electromagnetic radiation with wavelength below 10 angstroms (10^{-9} m) and generated by energetic electron processes. During interaction of X-rays with matter, X-rays possess intrinsic energy that may be imparted to the matter they interact with. Two main types of energy transfer that can occur when X-rays interact with matter are:

- Ionization, in which the incoming radiation causes the removal of an electron from an atom or molecule leaving the material with a net positive charge.
- Excitation, in which some of the X-ray's energy is transferred to the target material leaving it in an excited (or more energetic) state.

Theoretically there are several processes that can occur when X-rays interact with matter, but only three of these processes are important which are:

- Photoelectric effect
- Compton scattering
- Pair Production

Which process dominates is dependent on the mass absorption characteristics of the target (directly related to the atomic weight, Z) and the energy of the X-rays, shown schematically in the figure below.

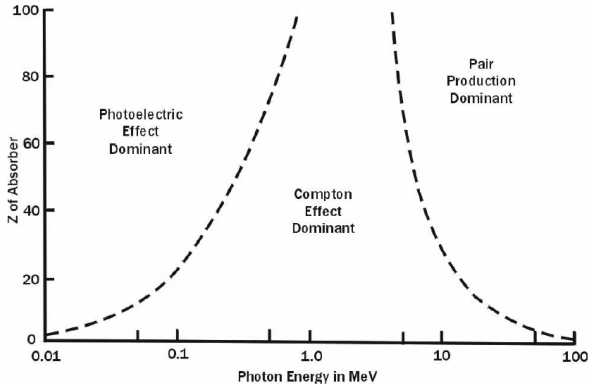

Figure 1.1: Photoelectric effect, Compton effect and pair production and their dominance at different energies and Z of absorber.

They all contribute to the attenuation of intensity when an X-ray beam crosses the matter. The phenomenon is described by the Beer-Lambert law :

$$I = I_0 e^{-\mu t} \tag{1.1}$$

Where I is the number of photons emerging from the target, I_0 the number of photons that hit the target and μ is the total linear attenuation coefficient illustrated by Fig 1.2.

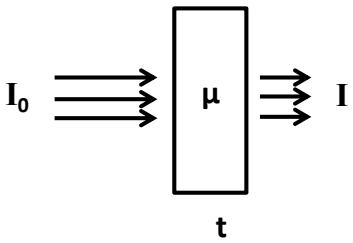

Figure 1.2: Illustrative scheme for the Beer-Lambert law.

Linear attenuation coefficient μ represents the sum of the coefficients related to three processes mention above: τ for photoelectric, σ for Compton and κ for pair production.

$$\mu = \tau + \sigma + \kappa \tag{1.2}$$

For the range of energies lower than 100 keV and for relatively low atomic numbers (Z 20÷50) the photoelectric effect dominates and it is possible to consider total linear attenuation

Coefficient only related to τ. In general for radiography the mass absorption coefficient μ/ρ (cm^2/g) are used, provided by NIST data base [7].

The Beer-Lambert law can be written:

$$I = I_0 e^{-\left(\frac{\mu}{\rho}\right)(\rho t)} \tag{1.3}$$

When an X-ray beam crosses a compound C the mass attenuation coefficient will be calculated as the sum of absorption of each element taking into account their weight fractions W_i:

$$\left[\frac{\mu}{\rho}\right]_C = \sum_i W_i \left[\frac{\mu}{\rho}\right]_i \tag{1.4}$$

Although the attenuation coefficient generally decreases with increasing photon energies, there are sharp discontinuities, known as absorption edges. The location of an edge along the photon energy axis depend on the atomic number of the absorber, and absorption edges have a number of important consequences, notably in the choice of a material as filters or intensifying screens [8].

The dependence of mass attenuation coefficient for X-ray with the energy for four elements it is presented in Fig.1.3 .The graph shows the decrease of mass attenuation coefficient when the energy is increased and also the K-edge discontinuity in correspondence of the photon interaction with K-shell electron.

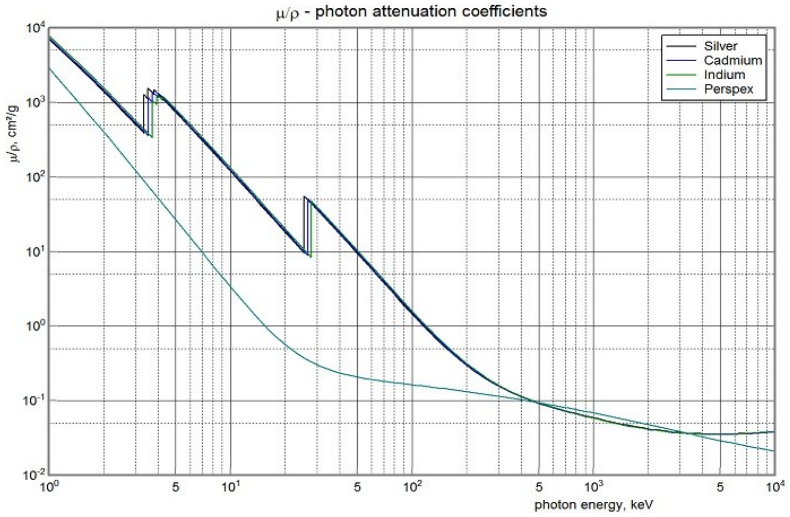

Figure 1.3: Silver, Cadmium, Indium and Perspex X-ray absorption coefficient.

1.3 K-edge filter subtraction technique

Monochromatic X-ray beams are ideal for several applications in medical radiography, industrial inspection and culture heritage. Synchrotron facilities produce monochromatic X-rays but their use is very expensive. For this reason the development of alternative technique using conventional X-ray tubes and *K*-edge filters are needed. We have developed a new technique to shape X-ray spectra with k-edge filters having the same transmission for energies lower than the *K*-edge. By subtracting digital radiographies of a sample obtained with such filters we are able to obtain quasi or pseudo- monochromatic radiographies.

1.3.1. Theory

Let us consider the energy spectrum φ(E) of an X-ray photon beam as the distribution of the photon flux with respect to the energy. The total photon flux φ [photons/second] will be given by the integration of the spectrum over the energy interval [E_{min}, E_{max}] where φ(E)≠0:

$$\varphi = \int_{E_{min}}^{E_{maX}} \varphi(E)dE \qquad (1.5)$$

If the photon beam is filtered with a material without *K*-edge in the energy range of interest [E_{min}, E_{max}], having an attenuation coefficient $\mu_f(E)$ and a thickness t_f the transmitted photon flux φ_f will be:

$$\varphi_f = \int_{E_{min}}^{E_{maX}} \varphi(E)e^{-\mu_f(E)t_f}dE \qquad (1.6)$$

Considering now a set of materials having photoelectric *K*-edge at energy E_{Ki} within the interval [E_{min}, E_{maX}] with attenuation coefficients $\mu_{K_i}(E)$ and thickness t_{K_i} chosen in such a way they satisfy the following conditions:

(1) the thickness t_{K_i} of each *K*-edge filter is such that the absorption is equal to that of the filter without K-edge for energies lower than the energy of *K*-edge E_{K_i}

$$\mu_f t_f = \mu_{K_i}(E)t_{K_i}, \quad E_{min} \leq E \leq E_{K_1} \qquad (1.7)$$

(2) the transmission of *K*-edge filters is negligible for photons with energy above *K*-edge

$$e^{-\mu_{K_i}(E)t_{K_i}} \cong 0, \quad E > E_{K_i} \qquad (1.8)$$

When conditions (1.7) and (1.8) are satisfied, it is possible to demonstrate that the subtraction of total fluxes of two filtered X-ray beams (φ_f) and (φ_{K_1}) will be:

$$\Phi_f - \Phi_{K_1} = \int_{E_{k_1}}^{E_{max}} \varphi(E)\, e^{-\mu_f(E)t_f} \qquad (1.9)$$

This means that the difference of total fluxes is equal to the flux of photons with energies higher than E_{K_1} in the beam filtered with no k-edge. If we consider now two *K*-edge filters with *K*-edge at energies $E_{K_1} < E_{K_2}$, both within the range [E_{min}, E_{max}] and thicknesses t_1 and t_2, respectively , satisfying conditions (1.7) and (1.8), it is straightforward to demonstrate that the subtraction of total transmitted flux φ_{K_1} to $\varphi_{K_2}$is:

$$\Phi_{K_2} - \Phi_{K_1} \cong \int_{E_{K_1}}^{E_{K_2}} \varphi(E) e^{-\mu_f t_f} \, dE \tag{1.10}$$

Equation (1.10) shows that the difference between the total fluxes transmitted by two properly selected *K*-edge absorbers is equal to the photon flux $\Phi_f \left(E_{K_2} - E_{K_1}\right)$ transmitted from the filter with no K-edge in the range of energy between the two *K–edge energies* E_{K_1} and E_{K_2} , (See Fig. 1.4).In other words, a single *K*-edge filtration works as a *low-pass filter* for photon energies with a threshold value equal to the *K*-edge energy, while the subtraction of the transmitted beam by two different *K*-edge filters satisfying conditions (1.7) and (1.8), can be used *as a band-pass filter* for photons with energy within the two *K*-edges.

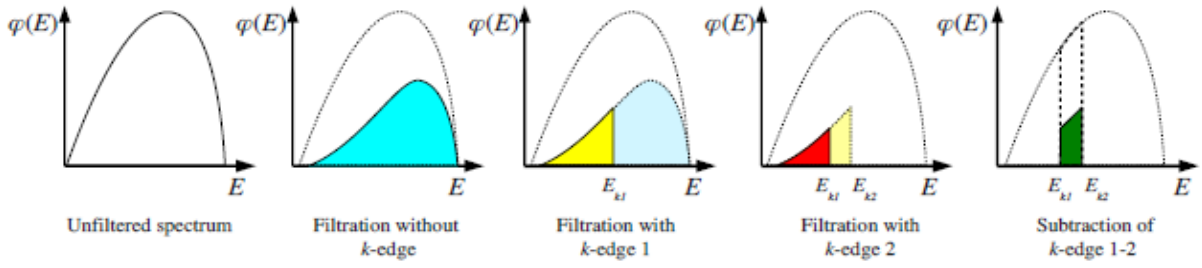

Figure 1.4: Schematic diagram of the *k*-edge subtraction technique.

Based on this theory, if we acquired the digital radiographies of a sample (or painting) by using properly chosen K-edge materials with a suitable detector, such as a Radeye200 CMOS pixeleted detector, subtraction between images will give quasi monochromatic images, presented as low and high energy image describe in paragraph 1.3.2. By processing images we can estimate the distribution of the target element in painting or sample test.

1.3.2. Analytical considerations in imaging with balanced filters

Let's consider the experimental setup for acquisitions of digital radiographies as below:

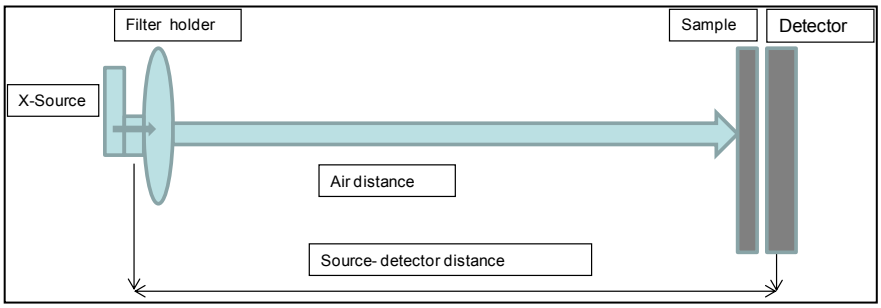

Figure 1.5: Instrumental setup for *K*-edge imaging.

Images acquired by an in indirect detector system that is a scintillator based x-ray detector, i.e RadEye200 CMOS detector coupled by a Gd_2O_2S (GOS) scintillator, will be modelled mathematically.

By supposing a sample placed between continues X-ray source and the detector (Fig 1.5), the average signal (image) $<S_{GOS}>$ obtained by CMOS sensor coupled by a GOS material will be:

$$< S_{GOS} >= \int_{E_{min}}^{E_{max}} \varphi_{0\,(E)}\, e^{-\sum_m \mu_{m(E)} t_m} \underbrace{\left(1 - e^{-\mu(E)^{gos} t^{gos}}\right)} \underbrace{\left(\frac{\mu_{en}^{gos}(E)}{\mu^{gos}(E)}\right)} E\gamma\, dE \qquad (1.11)$$

Where: $\varphi_0(E)$ is incident X-ray spectrum (photon fluence per energy interval), second term is the sum of the product of linear attenuated factor by thickness for each material that X-rays passes through, the terms underlined are respectively the fraction of photons attenuated in the detector and the amount of energy absorbed by the detector per attenuated x-ray photon , ($\mu_{en}^{gos}(E)$, $\mu^{gos}(E)$ are linear energy absorption and linear attenuation coefficients of the GOS scintillator (cm^{-1})), γ is conversion factor of detector (converting photon flux in gray values), E the energy for each incident X-ray photon in the range from E_{min} to E_{max}, and index m for all materials that attenuate the beam. Theoretical formula manly it is based on the absorption efficiency of the X-ray detector in which the signal is related to the total energy absorbed in the detector not in the number of X-ray photons [9].

If we have three *K*-edge filters (i.e., Silver, Cadmium, Indium), including *K*-edge target element (cadmium) with edge energy respectively $E_{k1} < E_{k2} < E_{k3}$, the image acquired by

detector for a sample positioned between source and detector for the first filter , I_{k1} , will be expressed as the integrated signal , S_m^1 with Eq. (1.12).

$$I_{k_1} = S_m^1 = \int_{E_0}^{E_{k1}} \varphi_{0\,(E)}\, e^{-\mu_{k1}(E)t_{k1}} e^{-\sum_m \mu_m(E)t_m} \underbrace{\left(1 - e^{-\mu(E)^{gos}t^{gos}}\right)} \underbrace{\left(\frac{\mu_{en}^{gos}(E)}{\mu^{gos}(E)}\right)} E\gamma\, dE \qquad (1.12)$$

Where $\mu_{k1(E)}$, t_{k1} are the linear attenuation coefficient (cm^{-1}) and thickness (cm) for filter material.

When we make the subtraction of images acquired for a sample using two edge filters that satisfy the conditions (1.7) and (1.8), the *low energy image* I_L in the energy interval $\Delta E = \left(E_{k_2} - E_{k_1}\right)$ tha is the difference between two *k*-edge energies, will correspond to integrated signal (ΔS_m^{12}) as follow:

$$I_L = \Delta S_m^{12} = \int_{E_{k1}}^{E_{k2}} \varphi_{0\,(E)}\, e^{-\mu_{k_2}(E)t_{k_2}}\, e^{-\sum_m \mu_m(E)t_m}\left(1 - e^{-\mu(E)^{gos}t^{gos}}\right) \left(\frac{\mu_{en}^{gos}(E)}{\mu^{gos}(E)}\right) E\gamma\, dE$$

$$\approx \varphi_{0\,(\bar{E})_L} e^{-\mu_{k_2}(\bar{E})_L t_{k_2}}\, e^{-\sum_m \mu_m(\bar{E}_L)t_m}\left(1 - e^{-\mu(\bar{E}_L)^{gos}t^{gos}}\right)\left(\frac{\mu_{en}^{gos}(\bar{E}_L)}{\mu^{gos}(\bar{E}_L)}\right) \bar{E}_L\, \gamma\, \Delta E \qquad (1.13)$$

Where $(\bar{E})_L$ is the mean energy value in the narrow interval defined by first two *k*-edge filters. Considering that energy range is too close (less than 2 keV), transitions are based on mean value theorem for the definite integrals in a closed interval. So we can consider that *low image* it is an image like acquired in a quasi monochromatic energy beam with a mean energy$(\bar{E}) \approx (E_{k_2} + E_{k_1})/2$).Integrated signal spectrally it is shown by gray histogram on Fig. 1.6.

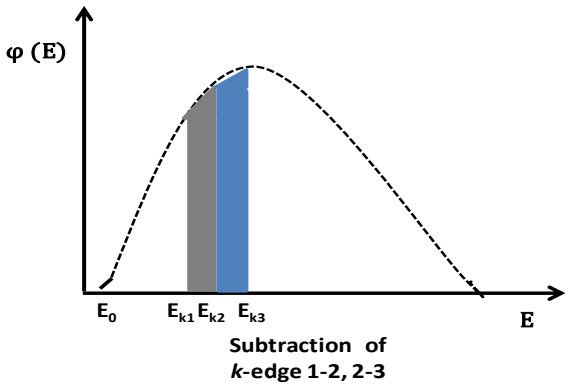

Figure 1.6: Pseudo-monochromatic spectra by using three adjacent balanced filters.

While for flat image that it is acquired when no sample it is between source and detector we can write:

$$I_L^0 = \Delta S_0^{12} = \int_{E_{k1}}^{E_{k2}} \varphi_{0\,(E)}\, e^{-\mu_{k_2}(E)t_{k_2}}\left(1 - e^{-\mu(E)^{gos}t^{gos}}\right)\left(\frac{\mu_{en}^{gos}(E)}{\mu^{gos}(E)}\right) E\gamma dE$$

$$\approx \varphi_{0\,(\bar{E})_L} e^{-\mu_{k_2}(\bar{E}_L)t_{k_2}}\left(1 - e^{-\mu(\bar{E}_L)^{gos}t^{gos}}\right)\left(\frac{\mu_{en}^{gos}(\bar{E}_L)}{\mu^{gos}(\bar{E}_L)}\right)\bar{E}_L\gamma\Delta E \qquad (1.13)'$$

In the same way we can write the expressions for the *high image energy*, I_H, and high flat image, I_H^0, which are integrated signals in the energy range $\Delta E = \left(E_{k_3} - E_{k_2}\right)$, above the k- edge of the target e element:

$$I_H = \Delta S_m^{23}$$
$$\approx \varphi_{0\,(\bar{E})_H} e^{-\mu_{k_3}(\bar{E}_H)t_{k_3}} e^{-\sum_m \mu_m(\bar{E}_H)t_m}\left(1\, e^{-\mu(\bar{E}_H)^{gos}t^{gos}}\right)\left(\frac{\mu_{en}^{gos}(\bar{E}_H)}{\mu^{gos}(\bar{E}_H)}\right)\gamma\, \bar{E}_H\Delta E \qquad (1.14)$$

$$I_H^0 = \Delta S_0^{23}$$
$$\approx \varphi_{0\,(\bar{E})_H} e^{-\mu_{k_3}(\bar{E})_H t_{k_3}}\left(1 - e^{-\mu(\bar{E}_H)^{gos}t^{gos}}\right)\left(\frac{\mu_{en}^{gos}(\bar{E}_H)}{\mu^{gos}(\bar{E}_H)}\right)\gamma\bar{E}_H\, \Delta E \qquad (1.14)'$$

Based on these mathematically modelled images we will introduce the procedure of corrections and processing images for obtaining information on element of interest in paintings.

1.4 Image processing

During the creation of a digital image from the detection of X-ray photons to the formation, there are several artefacts that cause either overestimation or under estimation of the signal level. These artefacts are noise and caused by different factors starting from the X-ray photons to the readout electronics, electromagnetic interference from external sources and the non linearity of CMOS detectors. For these reason image corrections it is necessary to avoid these noises [10].

1.4.1 Image corrections

For any images acquired by digital radiography the initial step is correcting them by two main artefacts: dark noise and fixed pattern noise (FPN).

- Dark field correction (offset)

The signal resulting from a solid-state detector it is affected by thermal noise as cause of

Thermal vibrations of charge carriers and depends on detector temperature and detection time. For this reason it is necessary subtracting the "dark image" by radiographic image, acquired at the same condition of time exposure when no X-ray photons hit the detector.

- Flat field correction (gain offset)

The fixed pattern noise (or structure noise) describes the spatially fixed variations in the gain across detector. The noise sources might be variation in sensititivity between the digital sensor pixel elements, the phosphor screen granularity, or inhomogenity of x-ray field. For correcting images from these effects it is used the flat-field image correction. To perform this correction radiographic images are normalized, pixel by pixel, by a white field image, acquired at the same condition of beam flux and energy, position and acquisition time, with no sample.
The conventional method to correct a row images (I) is:

$$I_{c_{E'}}(x,y) = \bar{g}_E \frac{I_{E',t_2}(x,y) - D_{t_2}(x,y)}{G_{E,t_1}(x,y) - D_{t_1}(x,y)} \qquad (1.15)$$

Where I_C is the corrected image, D is the averaged offset image(dark image) acquired for the same integration time, G is the averaged gain image (flat image) at the same irradiation condition and the same integration time, and $\bar{g}$ is the mean (or median) pixel value of G. The subscript E denotes the incident exposure, while the subscripts t_1 and t_2 indicate the times at which image sets are obtained [11].

1.4.2 Image subtraction and Lehmann algorithm

The principal of edge subtraction radiography is to make an *element specific image* using the absorbance image before (*Low energy image*) and after the absorption edge (*High energy image*) of the element of interest. By using conventional X-ray tubes *the low and high* energy image will be obtained by subtraction of three images acquired when the source is filtered by materials which have k-edge energies in the range very close to the element of interest and satisfied the conditions (1.7, 1.8 paragraph_1.3.1). Information on images, about the distribution of the element in a paint image, could be extracted in three ways; a) *linear subtraction*; b) logarithmic subtraction and c) *Lehmann algorithm (LA)*. The two first gives qualitative analysis while the last gives quantitative analysis (the surface density of target element in unit (g/cm^2). For evaluation of cadmium element, images will be processed by *linear subtraction*; and *Lehmann algorithm.*

- Linear subtraction (KES signal)

Considering the mathematical model of subtracted images obtained by integral detector CMOS the low and high images I_L, I_H (eq.1.13, 1.14) and flat low and high images, I_L^0, I_H^0, (eq.(1.13', 1.14') and supposing that we image a "Test sample" with a thickness t and a total linear attenuation coefficient of μ (for simplified the situation) we can write [12]:

$$\begin{cases} I_L = I_L^0 e^{-\mu^L t} \\ I_H = I_H^0 e^{-\mu^H t} \end{cases} \tag{1.16}$$

After correction of images (eq. 1.15), normalizing by flat image and making a linear subtraction of the low with high image, we obtain final KES image which it will depend on the linear attenuation of the k-edge element:

$$\left(\frac{I_L}{I_L^0} - \frac{I_H}{I_H^0}\right) = \Delta = \left(e^{-\mu^L t} - e^{-\mu^H t}\right) \tag{1.17}$$

- Lehmann algorithm

The dual energy algorithm introduced by Lehmann in medicine [13] consists of decomposing a single radiographic imaging into two components; the first one that gives the mass density distribution of the *K*-edge element $(\rho x)_{el}$ and the second one gives the mass density distribution of all other materials in the sample $(\rho x)_{matrix}$. To estimate the mass attenuation coefficient of the rest matrix a guess must be about the average composition. Often the rest matrix is represented by low Z equivalent material (water, carbon, Mylar, Perspex, etc.).Lehmann algorithm recently it is used for quantitative purposes in investigation of an element (pigment) in painting giving the mass density of element in (g/cm^2) [5], [14].

The signal in row images will be proportional to the number of photons that hit the detector after the transmission across the sample (Beer Lambert Law):

$$N(E_{\pm}) = N_0(E_{\pm}) \exp\left\{-\sum_j \left[\frac{\mu}{\rho}(E_{\pm})\right]_j (\rho t)_j\right\} \tag{1.18}$$

where $N_{(E\pm)}$ is the transmitted photons number per unit of area (correspond to image acquired for sample), N^0 incident photons number per unit of area (white field image), E_+ and E_- energies of monochromatic beams respectively above and below the K-edge of target element), $(\mu/\rho)_j$ are energy dependent mass absorption coefficients, $(\rho x)_j$ are the mass densities expressed in (g/cm^2) and the subscript j denotes all the elements that compose the sample under investigation.

Supposing that beam are monochromatic and with energies adjacent to *K*-edge of the target element means that mass attenuation coefficient of the target element will vary strongly comparing to the other elements $(\Delta\mu/\rho)_{el} \gg (\Delta\mu/\rho)_{matrix}$, that allow us writing the sum in (eq.1.18) as sum of absorption of the *target element (Cd)* and the absorption of all the other elements as PMMA [15].

$$\ln\frac{N_0}{N}(E_\pm) = \left[\frac{\mu}{\rho}(E_\pm)\right]_{Cd}.(\rho t)_{Cd} + \left[\frac{\mu}{\rho}(E_\pm)\right]_{PMMA}.(\rho t)PMMA \qquad (1.19)$$

If we explicit the expression (1.19) in two logarithmic equations respectively for Low(E_-) and High (E_+) energies and resolve the system with two unknowns that are the mass densities $(\rho t)_{Cd}$ and $(\rho t)_{matrix}$:

$$\begin{cases} \ln\frac{No}{N}(E_-) = \left[\frac{\mu}{\rho}(E_-)\right]_{Cd}.(\rho t)_{Cd} + \left[\frac{\mu}{\rho}(E_-)\right]_{PMMA}.(\rho t)PMMA \\ \ln\frac{No}{N}(E_+) = \left[\frac{\mu}{\rho}(E_+)\right]_{Cd}.(\rho t)_{Cd} + \left[\frac{\mu}{\rho}(E_+)\right]_{PMMA}.(\rho t)PMMA \end{cases} \qquad (1.20)$$

will be obtained two images as follow (1.21) and (1.22)

$$(\rho t)_{Cd} = \frac{\left[\frac{\mu}{\rho}(E_-\right]_{PMMA}.ln\frac{No}{N}(E_+) - \left[\frac{\mu}{\rho}(E_+\right]_{PMMA}.ln\frac{No}{N}(E_-)}{K_0} \qquad (1.21)$$

$$(\rho t)_{matrix} = \frac{\left[\frac{\mu}{\rho}(E_+\right]_{cd}.ln\frac{No}{N}(E_-) - \left[\frac{\mu}{\rho}(E_-)\right]_{Cd}.ln\frac{No}{N}(E_+)}{K_0} \qquad (1.22)$$

Where:

$$K_0 = \left[\frac{\mu}{\rho}(E_-\right]_{PMMA}.\left[\frac{\mu}{\rho}(E_+\right]_{Cd} - \left[\frac{\mu}{\rho}(E_+\right]_{PMMA}.\left[\frac{\mu}{\rho}(E_-)\right]_{Cd} \qquad (1.23)$$

In this way applying the algorithm for each pixels in the row images two final images are obtained: the target element image (Cadmium) and of the residual one (PMMA).
Based on this algorithm, applying it on images acquired by using balanced filters the equivalent parameters will be:

$$\underbrace{ln\frac{No}{N}(E_{-}) \leftrightarrow \ln(\frac{I_L^0}{I_L})}; \underbrace{ln\frac{No}{N}(E_{+}) \leftrightarrow \ln(\frac{I_H^0}{I_H})} \quad (1.24)$$

Where $I_L^0, I_L, I_{H,}^0$ I_L are expressed by equations (1.14, 1.14', 1.15, 1.15').

1.5 Cadmium pigments

K-edge subtraction technique reveals useful information especially an artist's techniques, pigments, and under paintings. Common elements in painting pigments are cadmium, mercury, lead, barium, antimony, and tin. Cadmium pigment has been chosen for investigation of *K*-edge imaging subtraction technique by using balanced filters.
The pigments of cadmium are inorganic colouring agents. Mostly used by the artists are cadmium yellow, cadmium orange and cadmium red which basically obtained by the cadmium yellow (cadmium sulphide) added some selenium in place of sulphur (cadmium selenide). The pigments are fine, discrete particles of coloured powder, with diameters of around 1 gm. The Cadmium pigments have also excellent heat stability which makes them essential in applications where elevated processing or service temperatures are encountered. It has been used by artists in contemporary age, since 1907. Artists who made frequent use of the yellow CdS pigments were Monet, Van Gogh, Miró, and Pablo Picasso. During the 20th century, the use of Cd pigments was expanded to include colouring of plastics etc. [16][17].

CHAPTER 2

2. X- Ray units and materials

In this chapter the base materials used for this work will be described with their specifications and the artefacts which will be in consideration to optimise them. The X – ray unit used for imaging was installed at Larix Laboratory, at Department of Physics in Ferrara.

2.1 X-Ray tube

X-ray source used is tungsten X-ray tube, M-143T manufactured by Varian[1] with 0.63 mm Beryllium window and a nominal focal spot size 0.1 x 0.35 mm^2. The X-ray tube is powered by a high-frequency 50 kHz, high-voltage generator, Compact Mammo-HF [2]with an adjustable voltage form 20 to 49kV. The setup for source has been chosen to obtain high flux by an anodic current, which is adjustable up to 120 mA.
Using Compact Mammo-HF allows working in two regimes: low current and high current.

- Low current (scopia)

This setting allows long exposition time, up to 300 second, and current supply is limited to low values, lower than 40 mA. Scopia setting is generally used for spectral analysis for a long exposition obtaining good statistics and low flux avoid saturation of the detector.

- High current (grafia)

Allows short exposition time, 5 seconds maximum, but current higher than 40 mA. High current is needed for imaging, by taking into account that balanced filters will be used for obtaining images.
For measurements of real values of output spectra of tungsten tube when nominal values are set up on Compact Mammo-HF[2] generator measurements are performed by CZT detector and it is calculated the endpoint energy spectrum by linear fitting using Igor program, presented in Tab. 2.1.

[1] Varian Medical systems

[2] Metaltronica Srl, Roma, Italy

Table 2.1: Nominal values and real values estimated for the X-ray unit used for imaging analysis.

Nominal values (kVp)	Output spectrum (keV)
25.0	29.6 ± 0.9
27.5	32.5 ± 0.8
30.0	36.2 ±1.1
32.5	37.6 ± 1.1
35.0	43.7 ±1.1
37.5	46.1 ±1.1
40.0	45.5 ±1.0

2.2 Filters selection

In order to investigate a K-edge element in paintings, i.e the cadmium element with *K*-edge energy at 26.7 keV, three *K*-edge absorber materials were chosen: silver (Ag), cadmium (Cd) and indium (In) having k-edge energies respectively of 25.5, 26.7 and 27.9 keV. Filters foils in dimensions 5cm x 5cm are covered by a mylar paper and embed inside of aluminium holder with a window 4.5 x 4.5 cm (Fig.2.1).

Figure 2.1 Filter foils Silver Ag, Cadmium (Cd), Indium (In).

Their thicknesses has been chosen in accordance to the conditions (1.7, 1.8) and reported on Table 2.2.

Table 2.2: Filters characteristics.

Material	k-edge energy (keV)	Ideal Thickness T (μm)	Real thickness T (μm)
Al	no k-edge	1550	1550 ± 50
Ag	25.5	109	102 ±1.0
Cd	26.7	127	129 ±1.2
In	27.9	141	147 ± 1.8

In additional an aluminium filter it is used for removing the lower part photons energy and shifted the mean energy of photons near to *K*-edge energy of interest (26.7keV).
By subtraction of images acquired by the RadEye200 detector using each filter the low image and high image energy will be in the range 26.5 - 26.7keV and 26.7- 27.9keV, approximated with mean energy 26.1 and 27.3keV, described on the Tab. 2.3.

Table 2.3: Pigments of Cadmium element and X-ray energies.

Element	Compound	Pigment name	K-edge energy [keV]	Low energy image	High energy image
Cadmium	CdSe CdS	Cadmium red Cadmium yellow	26.7	26.1	27.3

2.3 Phantoms and Test Pigments

For investigation of cadmium element in painting, canvas paint tests are prepared by Cultural Heritage Restoration and Conservation Centre "La Venaria Reale", in Turin, Italy and artificial phantoms are created in laboratory for the cadmium investigation as pure element.
These samples have been made with two main purposes: testing the technique ability to quantify the element content in the target and identify it when it is in different superimposed layers. The cadmium red tests have been realized on small canvas 10cm×10 cm in dimensions. The first one is divided in five sections with an increasing number of layers of cadmium pigment, as shown in Fig.2.2 [a]. In the second type two different pigments have been used, Cadmium red and Naples yellow (N.Y) and, in the central part of canvas, they have been superimposed as shown in Fig.2.2 [b]. Also a smaller target object, 10cm×8cm, has been realized with cadmium red pigment, in linseed oil on a mylar support Fig.2.2 [c].

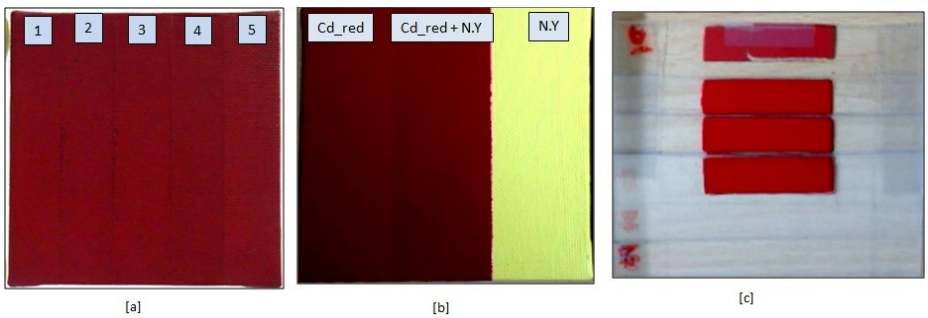

Figure 2.2: Test samples of cadmium red pigment.

For investigating the technique sensitivity for cadmium element (detection of minimal concentration by KES) also an artificial phantom is built in which 6pieces of pure cadmium foils with thickness in the range 35 to 130 μm are embed inside of two Perspex (PMMA) plates with dimensions 10cmx10cm with a thickness 0.6cm each shown in Fig_2.3.

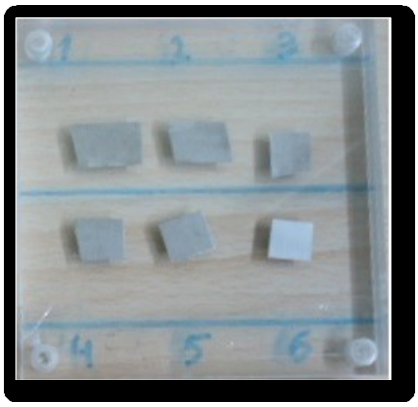

Figure 2.3: 6_pieces pure cadmium phantom.

2.4 Integrated long travel stage

In order to keep fixed and moving the test samples in front of detector a stepper-motor from Thorlabs' motorized stages LTS300[1] it is used. The linear translation stages are inclusive of the drive electronics which can either be driven via a PC or can be controlled manually.

LTS300 has a travel range 300mm with a maximum velocity 15 mm/s. The minimum incremental is 100 nm with a repeatable incremental movement of 4 μm. Absolute on-axis accuracy it is around 47 μm and the maximum percentage accuracy around 0.12 %. It has a maximum load capacity of 15 kg.

2.5 Detectors

The detectors used for investigation of k-edge subtraction technique have been CZT-100-XR as spectral detector and the remote RadEye200 (CMOS) imaging sensor.

2.5. 1 CZT spectrum detector

For measuring the spectra of tungsten (W) X-ray tube a cadmium zinc telluride detector (CZT) was used. XR-100T-CZT is a solid-state detector with 5x5x2 mm^3, 250 μm beryllium window and a resolution of 940 eV FWHM at 59.54 keV [18]. The detection

[1] ThorLabs-Integrated Long Travel Stages

efficiency is maximum between 10 and 80 keV and which means is approximately 100% in the energy range considered in this work with to maximum 44keV. In order to reduce the X-ray photon fluxes on the detector a pinhole with a diameter of 0.137 mm^2 has been used.

2.5.2 The imaging detector

The Remote RadEye™ 200 sensor manufactured by Rad-icon Imaging Corp (CA, USA), is a two-dimensional CMOS photodiode array featuring up to matrix 1024x1000 pixels, with an active area 98.4mm x 96mm and pixel pitch 96μm. It is design to high resolution radiation imaging for the energies range from 5 to 160 keV [19]. A Gd_2O_2S (DRZ-Std) scintillator screen it is placed in direct contact with the photodiode array which converts incident x-ray photons to light. Each sensor it is enclosed with an aluminium cover and a graphite layer that shields the sensor against ambient light and protects the sensitive electronics from accidental damage. The analogue video signal is processed, digitized to 12-bit resolution with a dynamic range 4000:1 at frame rates 1.35 frames per second and it is transmitted to a PC. All three interface modules are compatible with ShadoCam image acquisition software, in which the output signal is the digital count value per pixel (in ADU, Gray Level) averaged over several region-of-interest areas in the image. Summary of features of Radeye200 is reported in Tab 2.4:

Table 2.4: RadEye200 specifications.

Parameters	**RadEye200**	**Units**
Avg. Dark current (23°C)[(1)]	15	ADU/S[(2)]
Read noise (rms)	<1	ADU
Dynamic range	4000:1	
Digitization	12[(3)]	bits
Conversion gain	1400[(4)]	elec/ADU
Spatila resolution	5	Lp/mm
Max. frame rate	1.35	fps
x-ray energies	10-50	KVp
x-ray materials detecting materil (thickness)	Gd_2O_2S	46 m

[(1)]dark current doubles approx. every 8°C
[(2)]ADU = Analog-Digital Unit = 1 LSB (Least Significant Bit)
[(3)]14-bit option available (LVDS & Ethernet interface only)
[(4)] high-gain option (2x) available

CHAPTER 3

3. X-ray performance evaluation of remote RadEye200 CMOS sensor

Imaging with solid state detector brings different artefacts that affect imaging and for this reason it is important the evaluation of their performance. In the following section CMOS architecture, working principle and some physical parameters will be discussed.

3.1 CMOS image sensor

The first solid-state image sensors were the bipolar and MOS photodiode arrays developed in the late 1960s [20]. During the years (1970) the device, CCDs as an analogue memory quickly became the dominant image sensor technology. In the early 1980s, it was entered CMOS image sensors and the further advantage of technology scaling, the digital pixel sensor (DPS), integrates an ADC at each pixel made it the main silicon technology drivers.

The Figure 3.1 [21] [22] shows the structure of components of RadEye200 detector and the readout architecture of CMOS image sensor. CMOS sensor is direct coupling with a GOS (DRZ-Std) as scintillator. Two-dimensional array of Silicon photodiodes interface along with CMOS structures for scanning and readout. All support and control functions are integrated on-chip to minimize the amount of external circuitry needed to run the imager. The charge voltage signals from CMOS are read out one row at a time in a manner similar to a random access memory using row and column select circuits (see Fig 3.1 b).

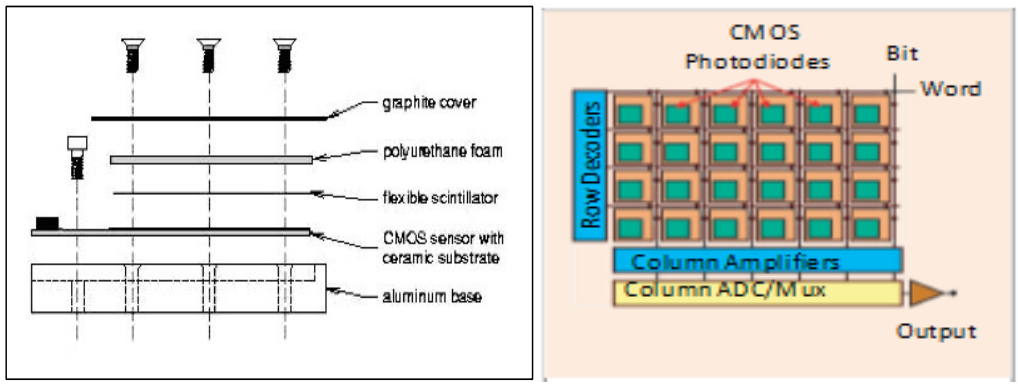

[a] [b]

Figure 3.1: (a) Cross section with scintillator (b) Readout architectures CMOS.

RadEye200 sensors works based on clock signal which is a particular type of signal that oscillates between a high and a low state, to a maximum frame rate of 1.35 fps.

The Vertical register is the photosensitive pixels, grouped in columns (in our detector

1024), which carried out collected charge at the end of the columns. The Horizontal register collects this signals and transfer charges to amplifier. The amplifier convert the charge derived from Horizontal register to a voltage signal.

3.2 Optimization of the system

There are a number of common metrics that are used for image sensors like quantum efficiency, dynamic range, conversion gain, dark current, well capacity[1]. Taking into account our purpose *in mapping elements* in an extended area of paintings it is necessary the evaluation of image sensor performance. Noises that affect more the signal in imaging are shot noise, fixed pattern noise, readout electronics, nonlinearity of CMOS sensor, etc..
Two main parameters can be important to be evaluated for optimizing CMOS image sensor: dark current and physical characteristics as MTF, NPS, DQE. In the following sections characterization in depth of the for dark current, MTF, NPS and DQE will be discussed.

3.2.1 Dark current

Dark current, i.e. charge generation with no incident light, is a parameter that is caused from electronic circuitry of the detector. It is a temperature dependent parameter and has a main affect in the linearity response or dynamic range of the sensor.
Also long exposure of detector vs. irradiation with x-ray will cause an increasing of the dark current and damaging the sensor. In that case the physical mechanism responsible for the increasing dark current is the charge build-up of positive charge in the oxide layer that directly modifies the underlying electric fields. Therefore modifying the charge density in the depletion region and increasing the leakage current across the PN junction of the diode. In a CMOS transistor it means that the threshold voltage of the transistor slowly shifts, until the device is either always on or completely closed off.
In addition electrons traps has been created by dose damage at the silicon- silicon dioxide interface which slowly de-trap into the pixel's potential well causing dark current to increase. Digital devices are able to tolerate moderate amounts of threshold voltage shifts, enabling them to continue to function normally until the transistors stop working and the device fails [23]. To obtain a good signal-to-noise ratio is necessary to minimize dark current

[1] http://www1.cse.wustl.edu/~jain/cse567-11/ftp/imgsens/index.html3

3.2.2 Physical characteristics performance

The performance of RadEye200 we will see in terms of the calculation of detective quantum efficiency DQE that shows the ability of the detector to transfer the squared signal noise to ratio (SNR) from the input stage to output stage, MTF that describes the signal response at a given frequency and NPS that describes the amplitude variance at given frequency.

3.2.2.1 Detective quantum efficiency theory (DQE)

The DQE shows the ability of the detector to transfer SNR from its input to the output. It is defined as the square of the ratio of output signal- to-noise to input to signal to noise [24]:

$$DQE = \frac{SNR_{out}^2}{SNR_{in}^2} \tag{3.1}$$

The input signal consists of x-ray photons, which generally obey Poisson statistics, the so for the input signal-to noise could be written:

$$\mathrm{SNR}_{\mathrm{in}}^2 = \left(\frac{\mathrm{q}}{\sqrt{\mathrm{q}}}\right)^2 = \mathrm{q} \tag{3.2}$$

While the output signal-to-noise ratio is commonly measured by observing the signal and the noise power spectrum at the detector output. Expressed in terms of the input signal and the detector gain G,will be:

$$SNR_{out}^2 = \frac{S_{out}^2}{NPS} = \frac{(q \cdot G)^2}{NPS} \tag{3.3}$$

By combining the above equations we get

$$DQE = \frac{q \cdot G^2}{NPS} \tag{3.4}$$

The detector gain and the noise power spectrum typically vary with spatial frequency. The modulation transfer function (MTF) is used to describe the relative decrease in gain with increasing spatial frequency. The final expression for calculating DQE then becomes

$$DQE(f) = \frac{q \cdot G^2 MTF(f)^2}{NPS(f)} \tag{3.5}$$

This expresses the fraction of input x-ray quanta used to create an image at each spatial frequency. The parameters as gain, MTF(f) and NPS(f) are easily measured simply by collecting enough images from the detector but input signal, it's more difficult. Usually requires the use of conversion tables and references, and it is more difficult when the incident x-ray photons have different energies.

3.2.2.2 Determination of parameters MTF, NPS, Gain of detector, DQE

In the following sections the determination of MTF, NPS, gain of detector and DQE for remote RadEye200 will be discussed.

- Modulation transfer function

An image sensor is a spatial (as well as temporal) sampling device. As a result, its spatial resolution is governed by the Nyquist sampling theorem that indicates: a continuous signal can be properly sampled, only if it does not contain frequency components above one-half of the sampling rate[1]. Spatial frequencies in line pairs per millimetre (lp/mm) that are above the Nyquist rate cause aliasing and cannot be recovered. Spatial resolution below the Nyquist rate is measured by the modulation transfer function (MTF), which is the contrast in the output image as a function of frequency.

The MTF of an idealized imaging system can be determined from the Fourier transform of the system's line-spread function (LSF). There are three experimental techniques to determine the LSF by a slit, wire, or edge imaging. [25], [26]. In the edge MTF technique, a "knife edge" made of a thin piece of strongly absorbing material is placed directly onto the detector and aligned at a slight angle typically (5-10°) to either the row or column direction. The edge should be as straight as possible (to within a fraction of the pixel size) and also as thin as possible to minimize shadowing in an off-axis measurement and scatter from the edge material at higher energies.

The measurements of MTF of radeye200 CMOs sensor it is used edge technique. Simply consists of taking an offset- and gain-corrected image of the edge using an appropriate combination of source kV, mA and integration time, in which we will have a good SNR. After correction of images (Eq.1.15), by making the differential along the row or column direction that is perpendicular to the edge, we obtain LSF of that particular row or column. The last step is to take the Fourier Transform of the LSF in order to obtain the MTF for the detector.

[1] $F_{Nyq}=1/2\Delta x$; Δx pixel pitch

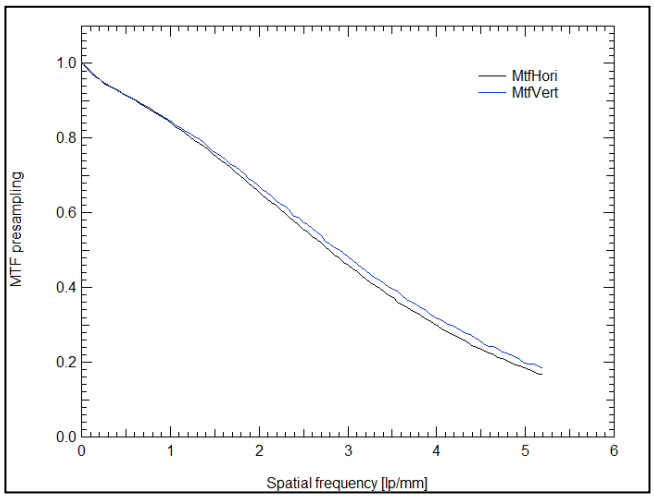

Figure 3.2: Presampling MTF for RadEye200 EV detector with GOS scintillator (Min-R Med).

The Fig. 3.2 represents MTF curves for the remote RadEye 200 CMOS imaging sensor. There is no significant difference between the MTF along the row direction and that along the column direction. By curves it seems that resolution of detector is 5.2lp/mm.

- Noise Power Spectrum

The Noise Power Spectrum describes the spectral decomposition of the noise variance in an image as a function of spatial frequency. It can be obtained by applying a two-dimensional Fourier Transform to an offset- and gain-corrected image from the detector. For the determination of NPS is enough to acquire two consecutive images from the detector and subtracts them. As NPS data are inherently noisy averaging over several data sets it is necessary in order to obtain a reasonably smooth curve.

If the two-dimensional NPS is symmetric, the analysis may be limited to either the row or the column direction by applying a one-dimensional Fourier Transform and averaging in the other dimension. This method yields a usable NPS curve from a single pair of images.

In Fig.3.3 are presented the experimental NPS curves for remote RadEye200 detector measured for various exposure levels. For signal nearer to maximum of dynamic range of detector NPS curves do not change too much in their values (see Fig 3.3). Might be that saturation of signal is achieved before the limit of dynamic range of detector (1:4000 ADU).

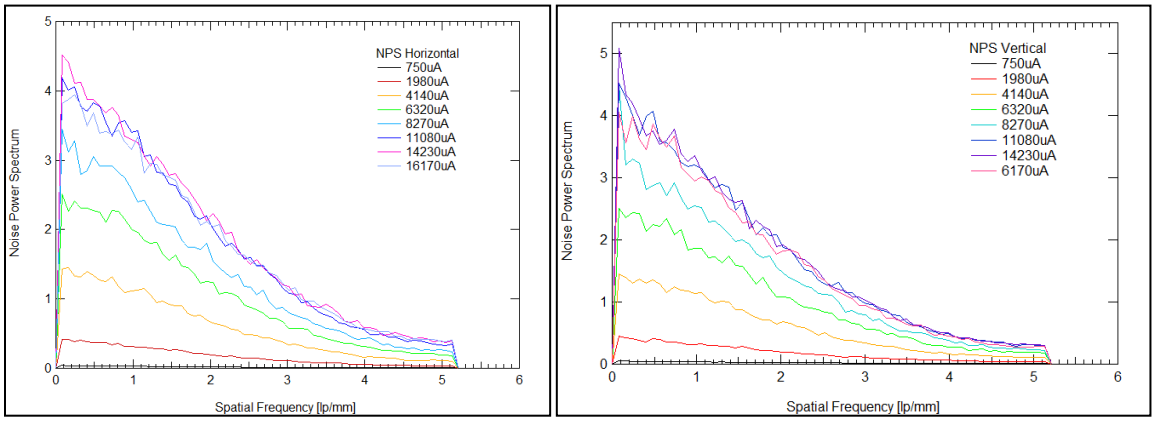

Figure 3.3: Experimental NPS curves in horizontal and vertical directions.

- Detector Gain

For determination of x-ray quantum flux incident on the detector two ways are possible: by measuring directly by ionization chamber or rely on physical models of the x-ray spectrum from a typical x-ray tube [1]. The magnitude of the resulting quantum flux then needs to be calibrated against an actual measurement taken at the position of the detector in the experiment.

For measuring the gain of Radeye200 CMOS sensor it is used a Mo-Mo X-ray tube, at 30 kVp. Output signal for different input X-ray flux is presented in the Fig 3.4. The plot of X-ray response of the RadEye200 sensor shows a slight "S" shape, which is characteristic of the detector's intrinsic response curve.

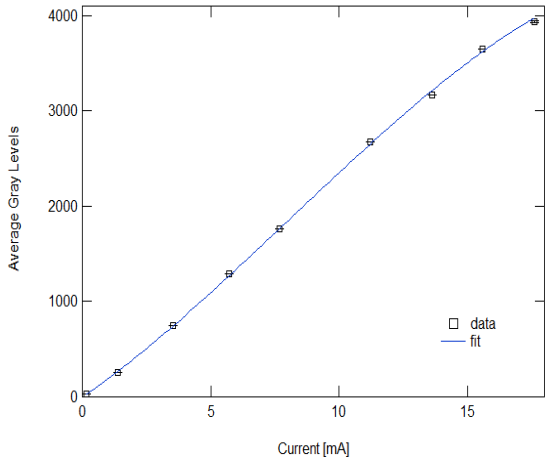

Figure 3.4: RadEye200 response curve to different x-ray output.

[1] Siemens X-Ray Toolbox; Rep.No78Spectrum processor (electronic Version)(D Sutton)

- Detective quantum efficiency

DQE is inverse proportional with NPS which express the distribution of the variance over spatial frequencies. After estimation of parameters the resulting DQE curves are shown in the Fig. 3.5 for RadEye200.

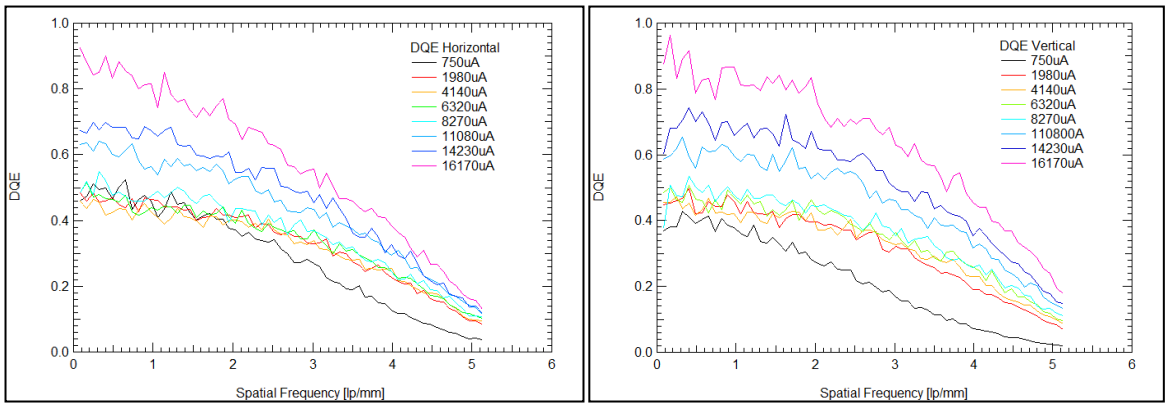

Figure 3.5: Frequency-dependent DQE curves for Radeye200 CMOS sensor.

CHAPTER 4

4. Imaging simulations

In this chapter image simulations for cadmium element using CMOS sensor will be described in additional to experimental tests to give definitions in analytical way of KES imaging technique by using balanced filters.

4.1 Image simulation for Cadmium pure element and Cadmium yellow

In order to estimate the real cadmium element in paintings, preliminary calculations have been performed for a similar situation like in the experimental tests.

Theoretical simulations will be discussed for a range of cadmium as pure element and as compound pigment, yellow cadmium CdS. Cadmium yellow it was chosen instead of red cadmium (CdS+CdSe) for simplify simulations. The target sample supposed it was Cd pure element or CdS as layers supported on a PMMA plate with a thickness 0.4cm.

Image simulations have been done considering experimental setup scheme for K-edge subtraction imaging (Fig.4.1), with an X- ray source Tungsten, filtered by Ag, Cd and In materials with correspondent thicknesses 0.102, 0.129, and 0.147mm and imaging receiver the integrator CMOS 200 sensor.

Figure 4.1: Experimental setup scheme.

Calculations were performed based on Eq. 1.12, which gives the average signal converted in image by a CMOS sensor coupled by a GOS scintillator. In additional an aluminium filter will be added for removing lower energy photons.

Filter thicknesses for Ag, Cd, and In are chosen satisfying the conditions (1.7 and 1.8) but are not perfectly in ideal one (the ideal thickness must be for Ag, Cd and In 0.109, 0.127 and 0.141 respectively). To achieve the ideal thickness for balanced filters (or Ross filters) it is difficult so some techniques are suggested by literature for correcting the balance errors [27, 28].

In our case a prefiltration with a low Z material (Al material) for Cadmium and Silver filtration was used. (The differences in transmitted spectra because of not ideal thicknesses are eliminated by adding an equivalent low Z material filters in additional to *k*-edge filter).

In this way the not overlapped spectrum transmitted by each k-edge filter in the range from the minimum energy till to their k-edge energy will be “disappear”, and a good

overlapping brings a good cancelation of photon energies out of band-pass defined by K-edge filters (refer to Fig 4.2). These two cases will be discussed below.

4.2 Theoretical Tungsten spectrum source and filtration spectra

For this purpose theoretical source spectrum for a W tube at 44 kVp, with anode angle 10 degree for time 1s is provided by Spectrum Processor[1], while the total attenuation coefficients μ/ρ (cm^2/g) for the materials that X- ray beam passes through, are taken from XMuDat[2].

In the Fig 4.2 Spectrum data for the tungsten source is presented graphically and filtered spectra are shown in sequent figure (Fig 4.3).

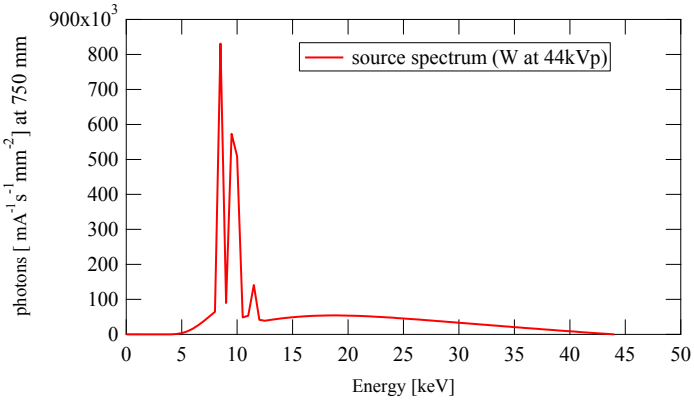

Figure 4.2: Theoretical W spectrum from spectrum processor at 44 kVp.

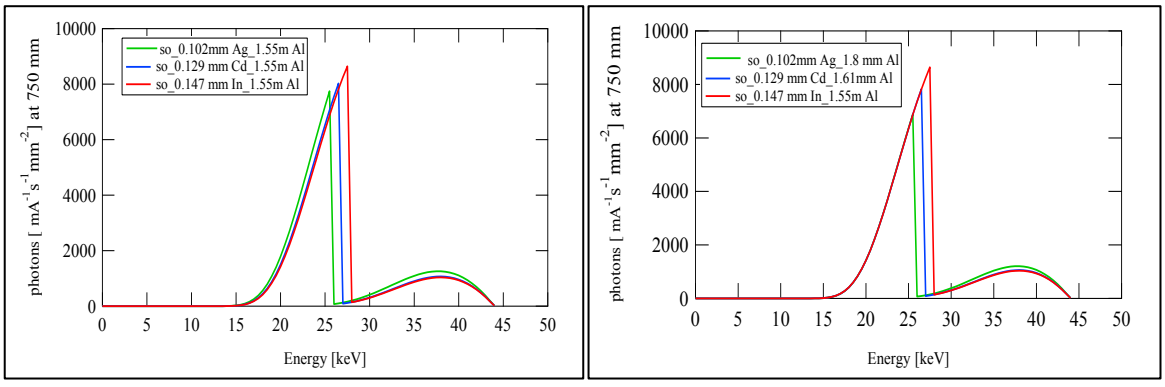

Figure 4.3: Theoretical W spectrum at 44 kVp filtered by Silver, Cadmium and Indium filter. Left: transmitted spectrum filtered by 1.55mmAl in additional to each k-edge filter (in correspondence with the colour). Right: transmitted spectra with k-filters+1.55mmAl and an additional for Cadmium filter of aluminium 0.06mm and 0.250mm for Ag.

[1]K Cranley, B J Gilmore, G W A Fogarty and L Desponds. Rep.No78.Catalogue of diagnostic X-Ray Spectra and Other Data, September, 97

[2]XMuDat. J Hubbel, S M Seltzer. NISTIR, 5632,1995

By Fig. 4.3 it is clear the effect of ideal of not-ideal thicknesses of material filters chosen.
First case when the source will be filtered by silver cadmium and indium filters with the thickness 0.102, 0.129, and 0.147 mm respectively and an additional filter of aluminium of 1.55mm (fig 4.3 left)
Second case when an additional aluminium filter will be added to silver and cadmium filtering (0.06 and 0.250mm Al respectively) which make the overlapping transmitted spectrum for the energy lower than k-edges energies (Fig 4.3 right), and considered better cancellation on subtracted images for photon energies lower than k-edge energies.

4.3 Image simulations and results

All simulations are performed using Excel program. In additional the theoretical spectrum is scaled by a factor for miliamperage (20mA), time integration of detector (1s), for the distance (inverse square low ($1/r^2$) and pixel area.
By using Eq. 1.12, once the FLAT and SAMPLE IMAGES are calculated, KES and LA it is applied. KES subtraction it is estimated as subtraction of Low Energy (Cd-Ag) with High-energy image (In-Cd), after some normalization (the high flat image $((\text{In-Cd})^0/(\text{In-Cd})^0)*(\text{Cd-Ag})^0$).
By applying direct the Lehmann algorithm we determine the mass density of Cd content in units (g/cm^2) .
Simulations have been performed for Cd pure and CdS in a range of thicknesses from 1 to 100 μm and as support a Polymethyl Methacrylate (PMMA) plate with a thickness 0.4cm. The energy chosen for Low and High image for applying L.A. was approximated to 26.3keV and 27.3keV.
Results obtained for both KES signal (cadmium distribution in Gl) and L.A (the mass densities of Cd element (g/cm^2) are presented graphically in Figures 4.3 and 4.4.

*First case***:** Fig.4.4 [a] presents the signals for KES in phantoms Cd+0.4cmPMMA and CdS+0.4PMMA and from it seems that the signal has an exponential dependency with increasing of thickness. A good linearity there is in the range of thickness 1 to 35 for Cd pure and around 100 micron for the pigment. For Lehman algorithm **(**Fig. 4.4 [b]) the response against Cd pure thickness it seems overestimated for values larger than 55 μm while for the pigment it shows linearity (signal increased proportional with the thickness)

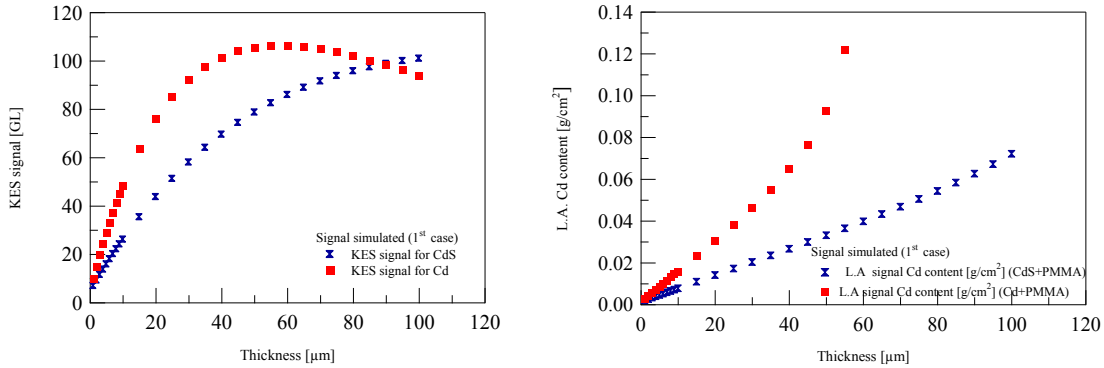

[a] [b]

Figure 4.4: Linear KES and LA signals for the phantoms Cd+PMMA (red markers) and CdS +PMMA (blue markers).(left) KES signal [GL] for both phantoms, [right] L.A. for mass density of Cd content in units [g/cm^2].

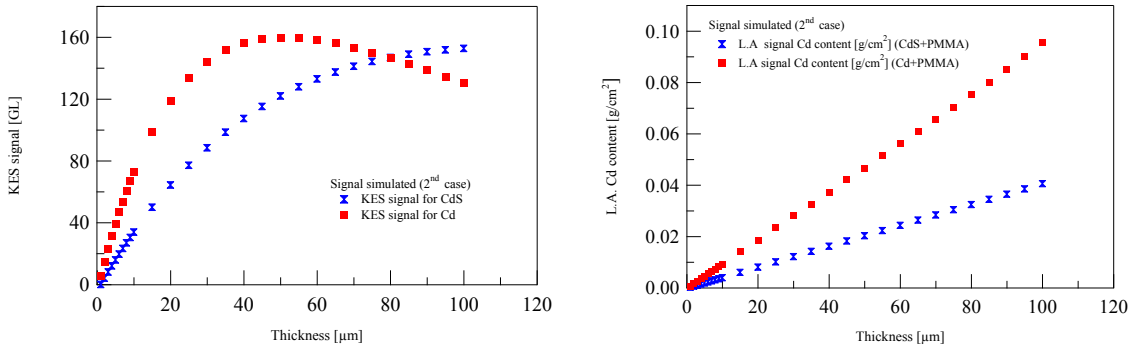

[a] [b]

Figure 4.5: Linear KES and LA signals for the phantoms Cd+PMMA (red markers) and CdS +PMMA (blue markers).[a] KES signal [GL] for both phantoms, [b] L.A. for mass density of Cd content in units [g/cm^2].

Second case: From results it seems that when a pure cadmium layer it is under investigation the signal response of CMOS detector it is linearly and more intensive in the region form 1 micron to 35 micron, and after than it reaches a maximum and fall down. That shows that for grater thicknesses there is no linearity but because of "self-absorption" it falls down. Theoretically this effect it is shown in chapter 1, (linear subtraction).

In case of pigment the range of linearity response of the system it is wider, in case of CdS more than 100 μm. When simulated images are processed by LA results shows a wider range of linearity for both Cd as pure element and its pigment CdS [Fig 4.5b].

By comparing two cases it seems that for the KES signal obtained when ideal thickness are used the signal is increased like a shift in all thicknesses in all the range, but not uniform.

An advantage of the method, when filter are ideally balanced, seems that it is capable to detect the element in very low dimensions, the range of microns, which can be useful in

NDT techniques applied in industry in discrimination of impurities of a k-edge element in an allow metal.

4.4 Experimental and theoretical simulations for the Cadmium 6pieces sample test

Experimental data and theoretical one are performed for filters used in the *first case* and *second case*. (Normalization is done with signal on PMMA). Experimental results shows good agreement with theoretical estimated.

Table 4.1: *First case*: Estimated values and experimental KES signal for 6 pieces cadmium pure.

Thickness (μm)	KES signal [GL]	KES signal estimated_th. [GL]	Realtive error [%]
38.2 ± 1.8	170.9 ± 9.9	163.3	4.4
50.4 ± 1.5	172.1 ± 10.3	172.6	0.30
55.7 ± 0.3	170.4 ± 10.11	173.7	1.9
64.5 ± 0.7	172.2 ± 9.25	172.8	0.36
72.9 ± 1.8	162.13 ± 10.1	169.8	4.7
121.6 ± 0.9	110.7 ± 7.8	135.4	22.3

Table 4.1': *First case*: Estimated values and experimental by L.A algorithm for 6 pieces cadmium pure.

Thickness (μm)	Cd_content (L.A_exp) [g/cm^2]	Thickness [cm]	Th._Cd_content (L.A exp) [g/cm^2]	Thickness [cm]
38.2 ± 1.8	0.042 ± 0.004	48.55	0.049	56.69
50.4 ± 1.5	0.051 ± 0.007	58.96	0.072	83.22
55.7 ± 0.3	0.055 ± 0.008	63.58	0.089	103.10
64.5 ± 0.7	0.071 ± 0.018	82.08	0.089	103.10
72.9 ± 1.8	0.066 ± 0.016	76.3	-	-
121.6 ± 0.9	0.052 ± 0.008	60.12	-	-

Table 4.2: Second case: Estimated values and experimental KES signal for 6 pieces cadmium pure.

Thickness (μm)	KES signal [GL]	KES signal estimated_th. [GL]	Realtive error [%]
38.2 ± 1.8	157.3 ± 10.1	124.3	20
50.4 ± 1.5	162.9 ± 11.2	128.4	21
55.7 ± 0.3	159.9 ± 11.1	127.9	19
64.5 ± 0.7	154.9 ± 9.8	125.5	19
72.9 ± 1.8	148.8 ± 16.1	121.6	18
121.6 ± 0.9	105.8 ± 9.7	90.6	14

Table 4.2': *Second case*: Estimated values and experimental by L.A algorithm for 6 pieces cadmium pure.

Thickness (μm)	Cd_content (L.A_exp) [g/cm^2]	Thickness [cm]	Cd_content (L.A_th) [g/cm^2]	Thickness [cm]
38.2 ± 1.8	0.035 ± 0.003	40.46	0.029	33.8
50.4 ± 1.5	0.044 ± 0.005	50.87	0.038	44.9
55.7 ± 0.3	0.050 ± 0.006	57.8	0.043	49.78
64.5 ± 0.7	0.058 ± 0.009	67.05	0.050	57.81
72.9 ± 1.8	0.060 ± 0.012	69.36	0.056	65.56
121.6 ± 0.9	0.060 ± 0.013	69.36	0.100	116.02

CHAPTER 5

5. Imaging

In this chapter primary will be described the spectral characteristics of the W x-ray tube with additional k-edge filtering used for the investigation of the cadmium element in paintings. Methodology of imaging and steps of elaborating images will be described in details. Results will be presented by a couple of images, graphically, tabulated data, and discussed.

5.1 Setup for tungsten X-ray source

In order to perform imaging for cadmium element with X - ray unit using the balanced filters spectral measurements have been performed by CZT detector. Measurements are performed positioning detector on a distance ~635 mm from the focal spot of the tube. In addition a small collimator with an area 0.137 mm^2 has been used in front of CZT detector. Preliminary measurement for the energy resolution of CZT detector has been done using the Americium - 241 as calibration source. The nominal energy resolution is indicated by datasheet only for 59.5 keV Am-241 peak energy.

The beam energy has been set at 35 kVp nominal value (44 kVp effective value) which include the K-edge energy of Cadmium. In order to make narrow bands of spectra in additional to k-edge filters (silver cadmium and indium) an aluminium foil it as added with thickness 1550 ± 50μm. Results are presented in term of counts rate (ph/s keV).

5.2 CZT energy resolution

In order to perform a complete characterization of the system, a preliminary measurement has been done to measure effective energy resolution of the CZT detector. As reference source have been taken Am-241 and measurement it is performed for 300s. Resulting spectra and correspondence channel energies are presented Fig 5.1.

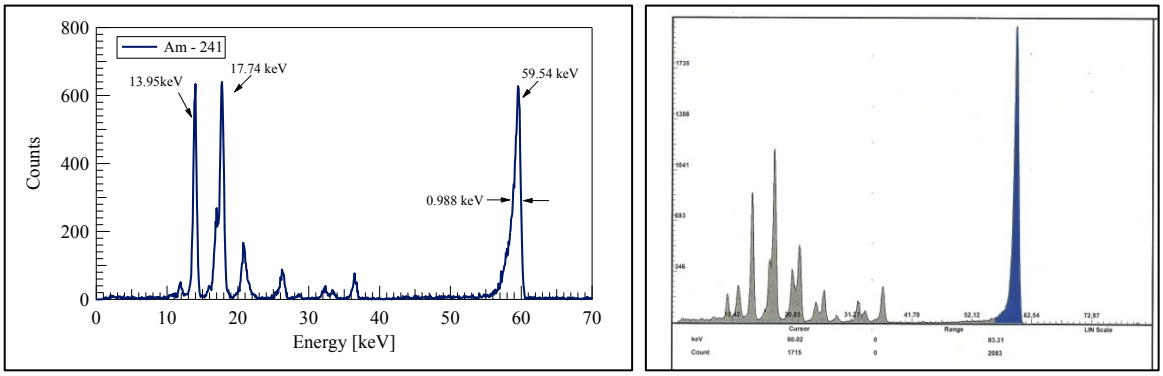

Figure 5.1: Spectra measured by CZT detector. Left: Experimental spectrum acquired by CZT for Am-241. Right: Theoretical spectrum.

Resolution of the detector for the 59.54 keV photon peak is 1.66 % approximately with theoretical one by the manual that it is 1.58%.

5.3 Spectral measurements

First case

Spectral measurements for tungsten X-ray tube and filtered by K-edge filters foils (silver, cadmium and indium) are performed with a nominal value set up at 44kVp.Spectrum is presented by Fig.5.2.

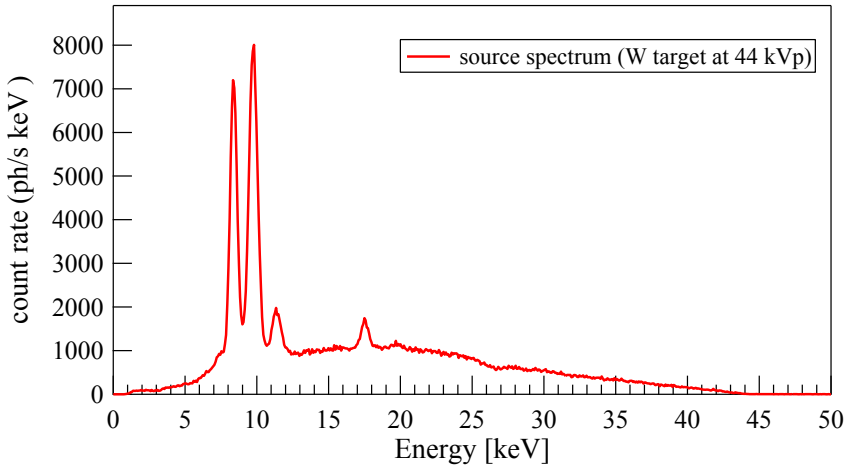

Figure 5.2: Output X- ray spectrum of Tungsten tube at 44kVp.

From spectrum measurement except to characteristic lines ($W_{L\alpha}$ $W_{L\beta}$ and $W_{L\gamma}$ it is visible and the presence of $Mo_{K\alpha}$. This is because of compose of the target tungsten with allow of molybdenum.

In the same conditions (energy peak 44kV), spectral measurements are acquired when the filters Silver Cadmium and Indium are placed in front of the output window of the tungsten x- ray tube presented on the Fig. 5.3.

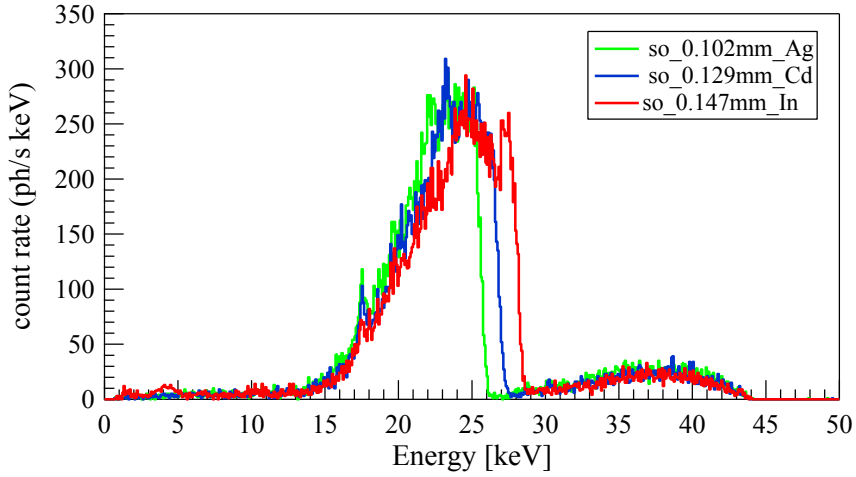

Figure 5.3: X- ray spectra transmitted by filter foils Ag, Cd and In (green-Ag, blue-Cd and red-In) at 44kVp.

For the reason that filters are not in ideal thicknesses it seems clearly by the graph that there is not a completely overlapping of transmitted spectra till to *K*-edges in correspondence. When we subtract the spectra (simple difference between spectral data of filter with grater k-edge energy with the spectrum of k-edge energy lower) there is not a full cancelation of the photon with energies out of interval energies defined by *k*-edge energies of filters (the "negative" values for photons before k-edge and some residuals photons for higher energies).

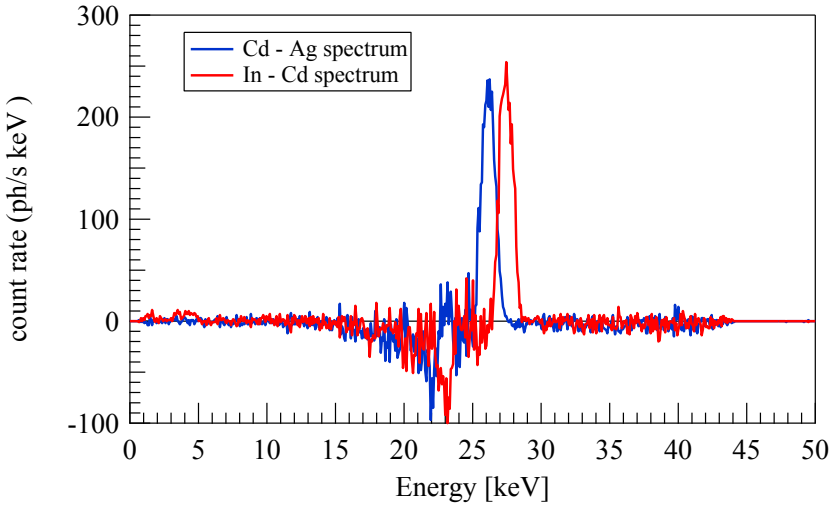

Figure 5.4: Subtracted X- ray spectra transmitted. The blue (Cd-Ag) spectra in energy range E = [25.5-26.7]keV; red [In-Cd] energy range E = [26.7-27.9]keV.

In that context there is an artefact that has to be considered in accuracy of our technique for investigation of cadmium element. Means that in our pseudo- monochromatic images will interfere even residual photons with energies grater or lower than energy ranges that define the low and high energy images.

In addition an Al filter with a thickness of 1.55 mm it is added in front of W source for each radiography to cut the lower energy photons and shift the mean photons energy near to the energy of interest (approximately to k-edge energy of cadmium element 26.7keV) illustrated on Figure 5.5 in (data provided by Spectrum Processor source).

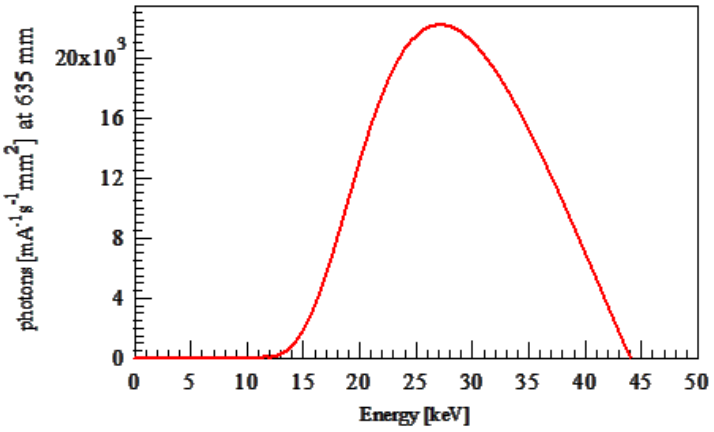

Figure 5.5: X-ray spectrum of a W-anode x-ray tube at 44 kVp, with 1.55 mm Al of additional filtration.

A resume of the characteristics of the W X-ray source and after filtered in terms of total flux, and mean energy photons, it is presented on Table 5.1.

Table 5.1: Total number of photons and the mean energy for W spectra and attenuated one by filtration at 44kVp.

X-ray spectra	Total number of photons [counts]	Mean energy [keV]
Tungsten source (W)	443332	16.80
W_attenauted by Silver foil (102 μm)	25716	23.55
W_attenuated by Cadmium filter(129 μm)	26754	23.96
W_attenuated by Indium filter(147 μm)	28274	24.05

The mean photon energy is calculated as ratio of the sum of product of number of photons with each energy bin with the total photons number (Eq. 5.1) .

$$E_{mean} = \frac{\sum_i N_i E_i}{\sum_i N_i} \qquad (5.1)$$

Second case

Spectral measurements with adding prefiltration in additional to Ag and Cd filter are presented in Fig 5.6 and Fig 5.7 for a longer time acquisition than in first case. Is obvious that in this case we have a better overlapping of transmitted spectra by each k-edge filter till to their *k*-edge energies. In spectrum transmitted by Indium filter is present a photo peak at the energy 4.1keV which correspond to the Cd escape peak from the detector CZT (Cadmium Zinc Telluride).

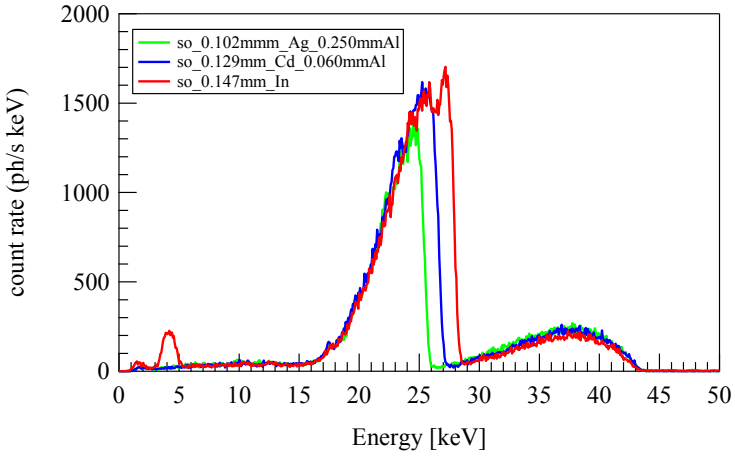

Figure 5.6: Transmitted spectra by filter foils Ag, Cd and In when 0.250mm and 0.060 mm Al are added for Ag and Cd respectively for W at 44kVp.

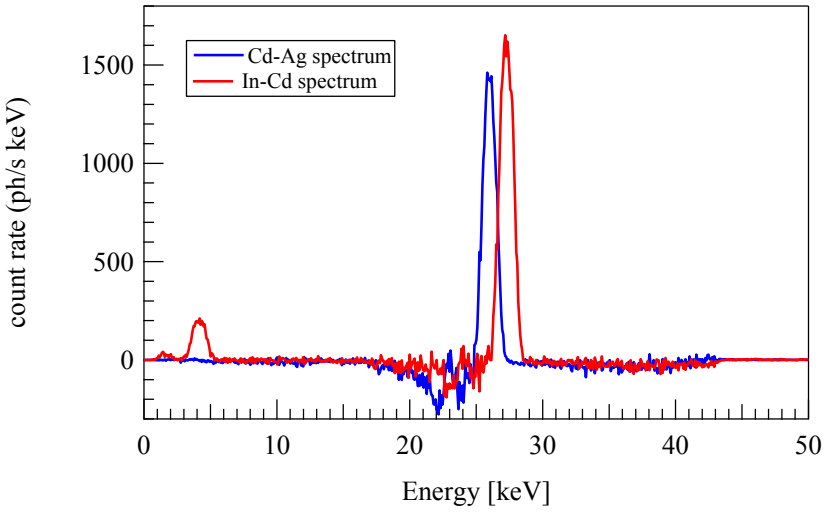

Figure 5.7: Subtracted X- ray spectra transmitted by filtering a W tube at 44kVp. The blue (Cd-Ag) spectra in energy range E = [25.5-26.7]keV; red [In-Cd] energy range E = [26.7-27.9]keV.

5.4 Imaging cadmium element

Investigation of cadmium element by using K-edge subtraction technique with balanced filters has been performed on different test objects, detailed in the chapter 2.
By using these different samples we will test the technique capability in order to quantify the element qualitatively and quantitatively.
Imaging of samples has been done for the same setup on W tube at the energy 44kVp and three radiographies has been performed for each sample test by adding filters foils Silver , Cadmium, Indium in front of tube.
Once obtained images, are corrected for the gain and offset and processed by using linear subtraction and L.A. using ImageJ software[1].

5.4.1 Cadmium pigment test samples

Three main tests of cadmium red pigment are investigated and will be considered in the following.

5.4.1. 1 Cadmium red 5sections

The test object it's a small canvas, 10×10 cm, with an increasing number of superimposed cadmium red pigment layers from 1 to 5 (detailed in Chapter 2). Paint colour contains 2.1g pigment + 2.1g binder.
Three radiographs are acquired with remote RadEye200 CMOS sensor, at the energy peak 44kVp, with anodic current 20 mA and an exposure time of 1 second.
Corrected images are presented in Fig. 5.8 in correspondence with filter used in front of tungsten tube.
Row images (corrected only for offset and gain) has an analogue digital signal in gray level proportional with photon fluence that hit the detector. From images, the third radiography, indium one, is more brighter as it is expected because more photons hit the detector considering that the spectrum cut-off edge of In is greater than Cd and Ag filters (the same reasoning is for the cadmium image versus silver image).
(k-edge energies $E_{k\,(In)}$=27.9 keV In, $E_{k\,(Ag)}$ =25.5 keV, $E_{k\,(Cd)}$ =26.7keV).

[1] ImagJ 1.45S. W.Rasband. National Institutes of Health, USA. http://imagej.nih.gov/ij

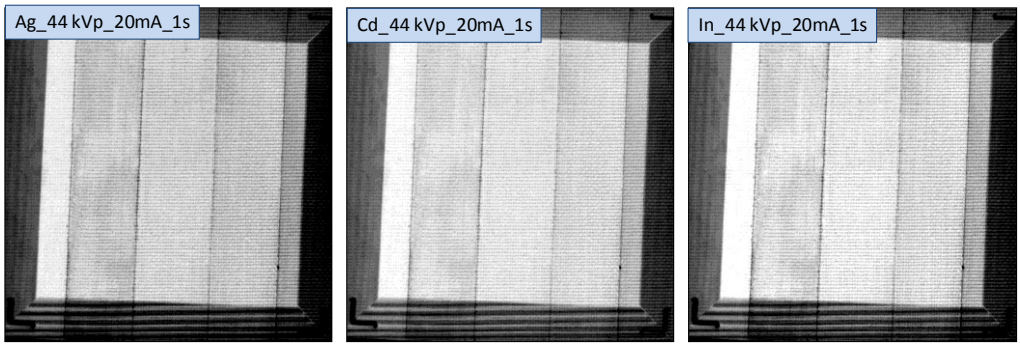

[a] [b] [c]

Figure 5.8: Images of 5section Cd_red canvas test by using W x-ray tube with additional balanced filters. [a] Image acquired with Silver 0.102 mm; [b] Image with Cadmium filter 0.129 mm; [c] Image with Indium 0.147 mm.

Linear subtraction (KES signal)

In linear subtraction, the low energy image is subtracted from high energy image without logarithmic transformation. For obtaining the Low and high energy images it is made the difference of images acquired with the filters Silver, Cadmium, and Indium. Quasi-monochromatic images are obtained after subtraction of three filtered radiographies with a mean energy 26.1keV for Low Energy (L.E) and 27.3keV for High Energy(H.E) Images, presented in Fig. 5.9 [a][b]. The Low Energy image contains the information for energy photons in the interval [25.5keV - 26.7keV] and shows almost uniform gray level (signal) in whole canvas and darker in areas where wood frame of canvas is present (higher attenuation). The High Energy image H.E obtained by the difference of Indium with Cadmium is presented in Fig. 5.9 [b].

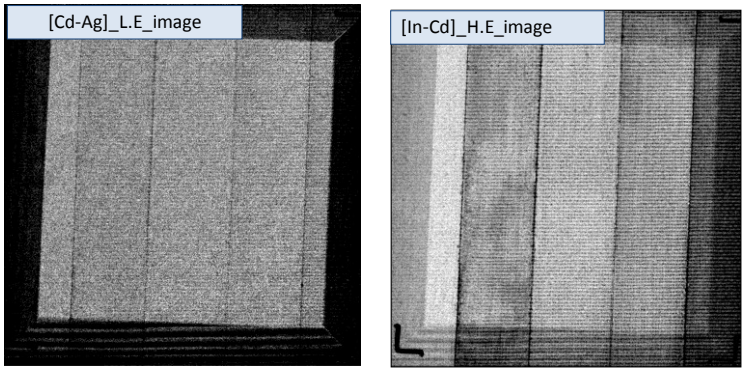

[a] [b]

Figure 5.9: [a] Low Energy image (Cd-Ag image), [b] High Energy image (In-Cd image).

The H.E image shows the difference on gray level on 5sections of canvas test in accordance to the cadmium red layer superimposed on each section in accordance to the theoretical considerations, i.e. mass attenuation of k-edge element have maximum

variation in energy range just below and after its k-edge energy, that means that differences in signal to each section correspond to the presence of cadmium element (more bright means more transmitted photons through the sample - less dense or less thick sample when the matrix is one element).

The final step, the difference between L.E and H.E image presented in Fig. 5.10 [a], gives the cadmium distribution on whole image of canvas test.

In Fig.5.10 [b] the plot of Cd content along all the canvas, on the selected region is shown.

In Fig.5.10[c] the Cd mean values in the sample are displayed. Error bars are the standard deviation of the mean cadmium content. Values are tabulated in the Table 5.2.

The results show not an increasing layer of cadmium content, and also not uniform layers along the whole canvas red test. The presence of cadmium content also will be confirmed in consecutive chapters (chapter 6) by non quantitative XRF analysis.

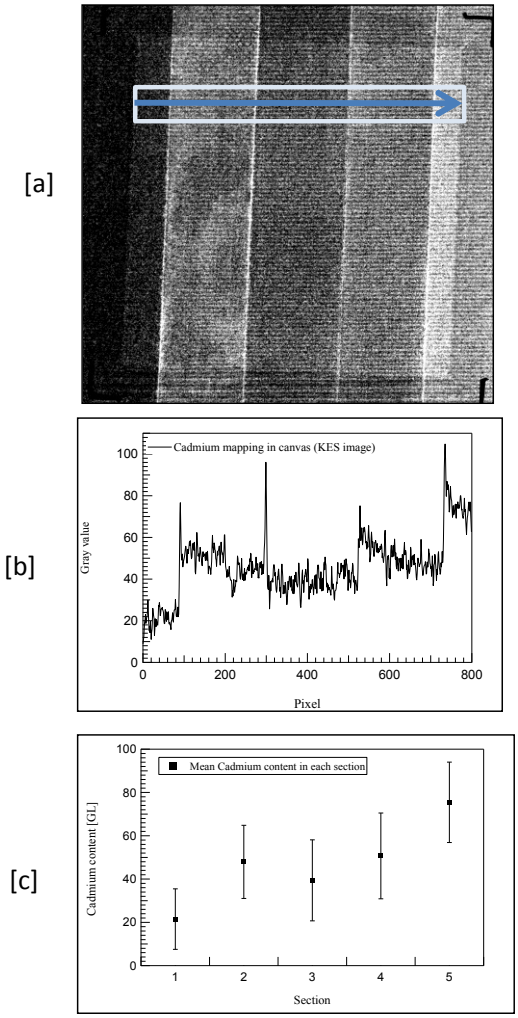

Figure 5.10: [a] Cadmium distribution image by KES subtraction of 5section canvas test. [b] plot of Cd content along all the canvas test at selected region. [c] the Cd mean values in each section.

Table 5.2: The mean values on each section are presented their standard deviation.

KES signal	Mean [GL]	σ_{mean} [GL]
section_1	21.5 ± 13.9	0.25
section_2	47.9 ± 16.8	0.19
section_3	39.4 ± 18.7	0.20
section_4	50.7 ± 19.8	0.22
section_5	75.4 ± 18.6	0.37

Lehmann algorithm

Results after processed images by Lehmann algorithm are shown in Fig 5.11 and Fig 5.12 in the same way as for linear subtraction of images (KES), for quantitative purpose.

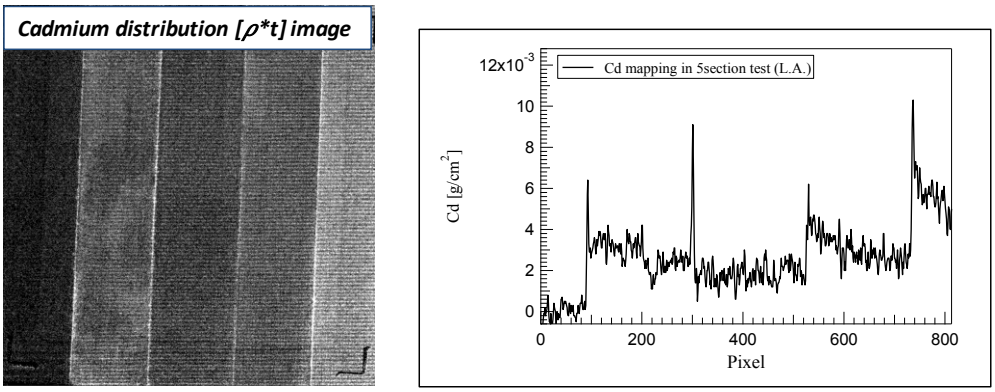

Figure 5.11: Image and the plot profile of image for cadmium content.(left) Cadmium distribution image by L.A. (right) Plot of Cd content along all the canvas test at selected region.

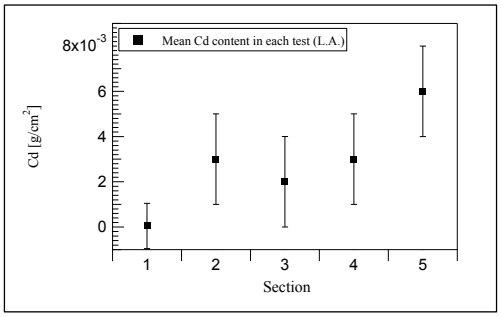

L.A results	Cd content [g/cm^2]
section_1	4.51E-05 ± 0.001
section_2	0.003 ± 0.002
section_3	0.002 ± 0.002
section_4	0.003 ± 0.002
section_5	0.006 ± 0.002

Figure 5.12: Cd mean values in each section of canvas test and tabulated data.

Measurements have been performed on Cd red 5 sections sample with adding prefiltartion in front of Ag and Cd called as *second case* (mentioned in chapter 4).

KES and Lehman results are presented in the same way as in *first case.* Comparing to previous results, after normalisation for KES signal the noise it is increased (standard deviation measured on images in GL). Also the results come lower in values.

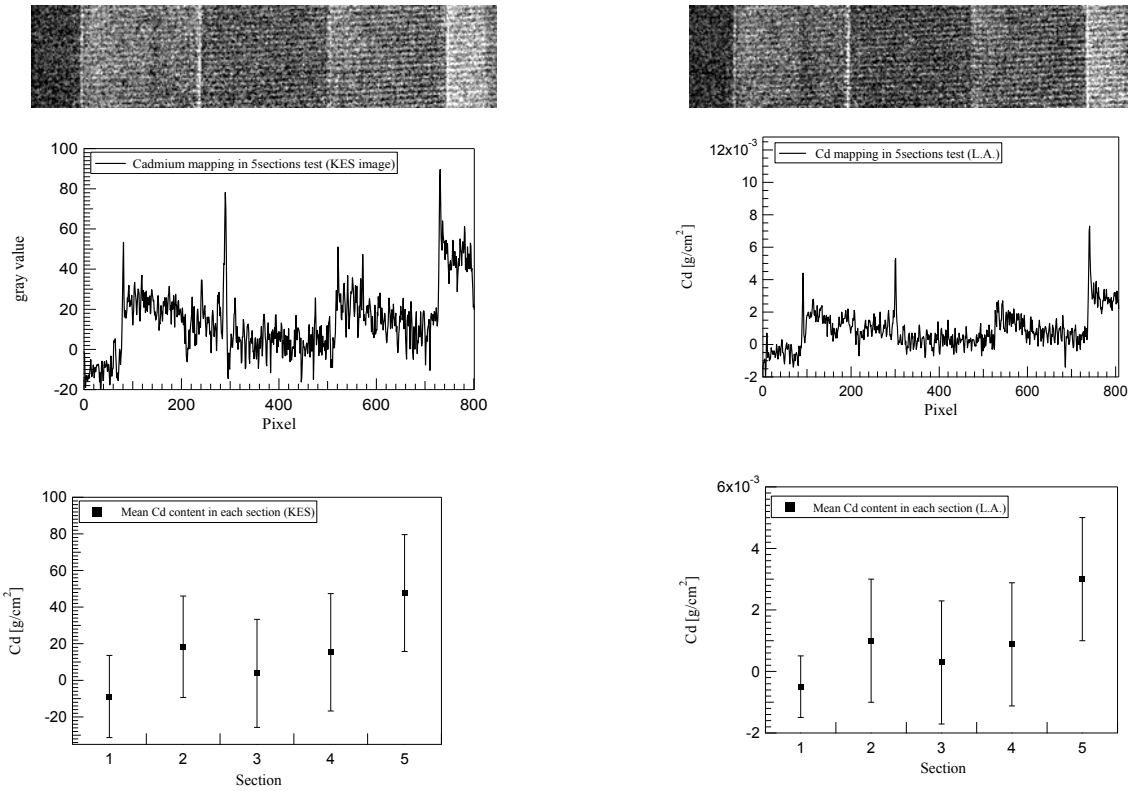

Figure 5.13: Images and Cd content in a selected region on image for second case. (Left) KES results for cadmium content (right) L.A mean values in each section of canvas test 5section Cd red.

Table 5.3: The Cd mean values for KES and LA (second case) for 5section Cd red sample

5sections Cd red test	Mean [GL]	Cd content [g/cm^2]
section_1	-8.9 ± 22.4	-0.0004 ± 0.001
section_2	18.3 ± 27.7	0.001 ± 0.002
section_3	3.8 ± 29.5	0.0002 ± 0.002
section_4	15.3 ± 32.05	0.0008 ± 0.002
section_5	47.6 ± 31.9	0.003 ± 0.002

In following the cadmium mapping on tests samples and painting will be presented only for *the first case*.

5. 4.1.2 Cadmium red 4 strips

Another target object has been realized with a different Cadmium Red pigment and a different number of superimposed layers of pigments.

The sample has been analyzed by using same the energy, KVp and current settings of previous analysis. Target object is with an increasing number of superimposed pigment layers, from 1 to 4, of Cadmium Red (CdS + CdSe, Kremer pigments n. 21140), on mylar support. Imagings acquired by Radeye200 CMOS sensor are shown in the Fig.5.14, and subtracted images in Fig.5.15.

A comparison between the linear subtraction and Lehmann algorithm is presented.

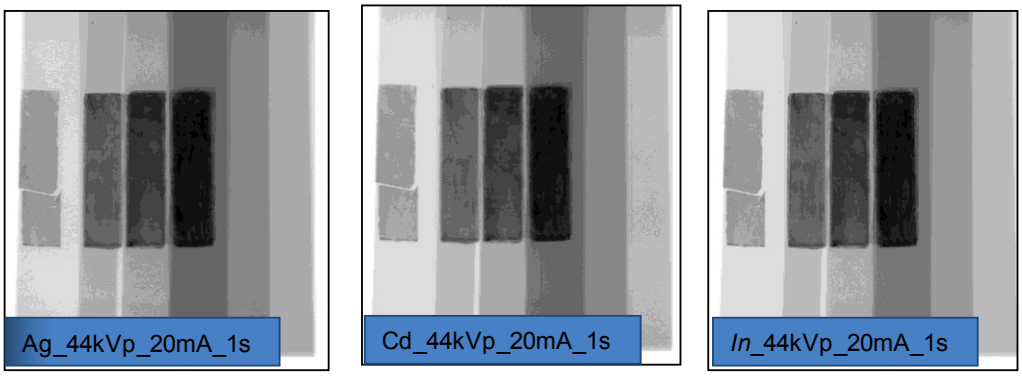

Figure 5.14: Images of 4strips Cd_red on mylar support. [a] Image acquired with Silver 0.102mm; [b] Image with Cadmium filter 0.129 mm; [c] Image with Indium 0.147mm.

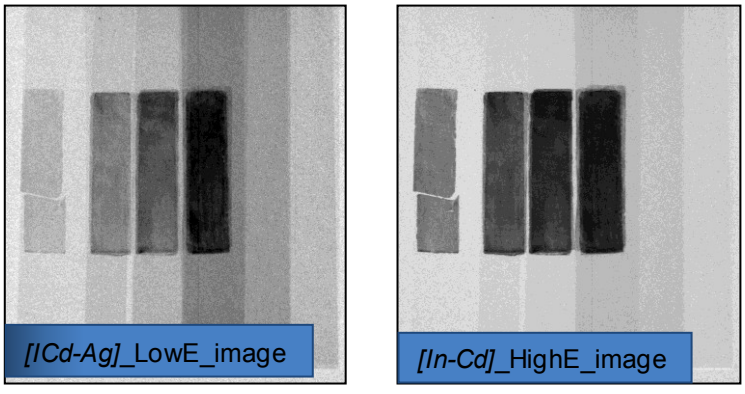

Figure 5.15: [left] Low Energy image (Cd-Ag image) [right] High Energy image (In-Cd image).

Linear subtraction images (KES image*)* presented in Fig 5.16. L.A results are presented on Fig.5.17.

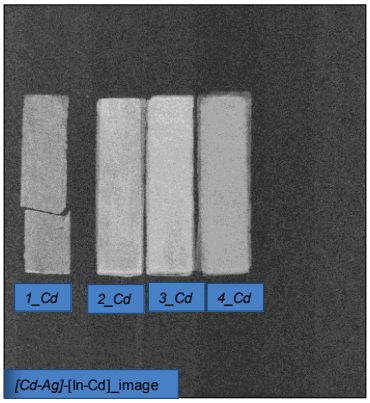

[a]

[b]

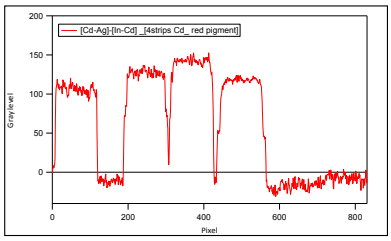

[c]

Cd_layers	Mean [Gl]	Area [pixel²]
1	104.59 ± 9.26	6844
2	131.79 ± 11.26	
3	142.33 ± 13.28	
4	117.03 ± 14.27	

Figure 5.16: KES results.[a] Image of Cadmium distribution (GL units [b] Mean Cadmium [GL] content detected in each section, [c] results tabulated for each strip.

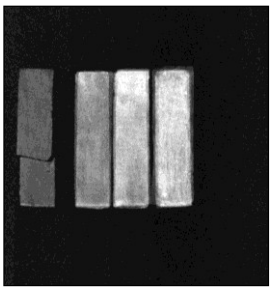

[a]

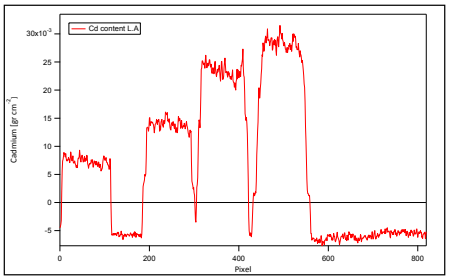

[b]

Cd_layers	ρ*t [g/cm²]	Thickness [⍰m]
1	0.007 ± 0.002	8.09
2	0.016 ± 0.003	18.50
3	0.024 ± 0.003	27.75
4	0.025 ± 0.003	28.90

[c]

Figure 5.17: L.A results. [a] cadmium distribution image (g/cm^2), [b] Mean Cadmium [GL] content detected in each section, [c] results tabulated for each strip.

From results the KES gives increasing value form layers 1 to 3 but then it is lowered that it is not compatible with real layers of cadmium present. By applying L.A the mass density of cadmium on the fourth layer it comes in increasing values as it in correspondence to real layers on sample.

5.4.1.3 Yellow Naples + Cadmium red

For the test sample Cd red and Y.N which is a combination of these two pigments as described in chapter 2. Imaging is performed for the same experimental setup, at 44kVp and 20mA. Images after elaborated by KES and L.A algorithm are presented in (Fig. 5.18). On final images obtained a map of cadmium element, on a selected region, is presented in Fig 5.19. Also the mean values are presented in the Table 5.4.

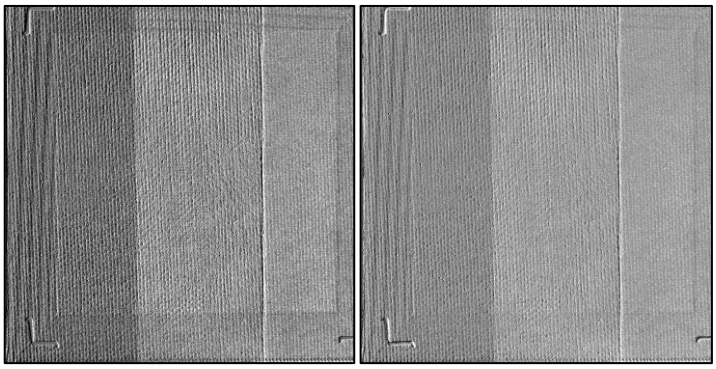

Figure 5.18: Cadmium distribution images for Y.N +Cd Red test canvas after processing. (KES and LA processed)

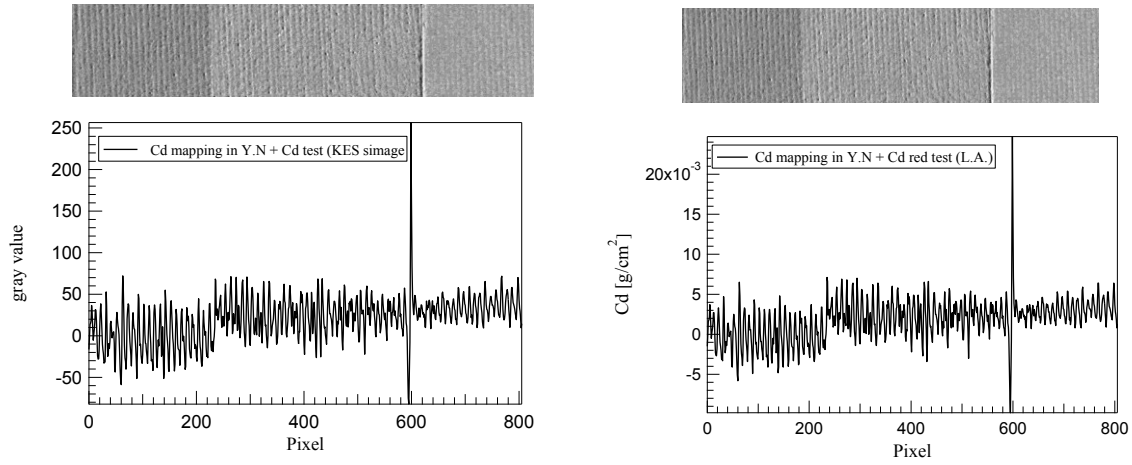

Figure 5.19: Cadmium mapping on images of Y.N+CdRed**.** [Left block] Mean Cadmium [GL] content detected along whole the canvas test by KES. [Right block] Cd content in (g/cm^2) by L.A. signal.

Table 5.4: The Cd mean values on each section of images processed by KES and L.A for Y.N + Cd redsample.

Y.N+Cd_red ($(Pb_2Sb_2O_7$ + (CdS+CdSe))	Mean [GL]	Cd content [g/cm^2]
Y.N	-0.66 ± 39.85	-0.0002 ± 0.004
Y.N+ Cd red	24.15 ± 42.01	0.002 ± 0.005
Cd red	34.25 ±24.49	0.003 ± 0.002

By images and results obtained it seems that the presence of lead (as component of Yellow Naples) in first two sections, gives a high noise in images and it is shown by both methods linear KES and L.A. Another artefact affecting image is the non uniformity of pigments spreaded in canvas texture.

5.5 Cadmium 6pieces sample test

In order to preestimate the real pigment on paintings artificial phantom 6pieces of Cd pure metal foils, with knowing thicknesses, has been studied. The linear KES subtraction has been applied by using normalization over flat images. Results are presented by images (row images in Fig 5.20 and final KES image in Fig. 5.21) and the signal extracted on each metal foil in a region 100x100 pixel, graphically plotted (Fig 5.22).

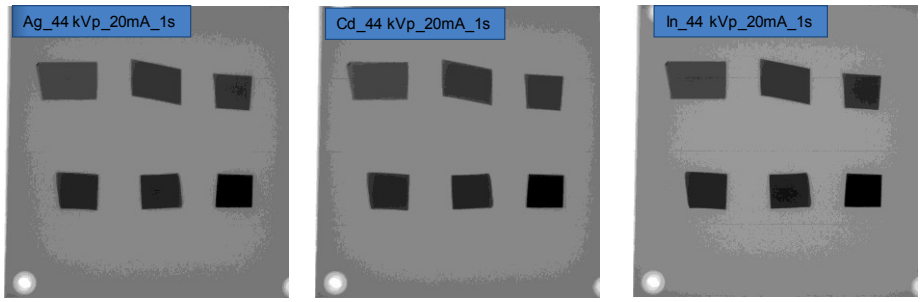

Figure 5.20: Images of 6pieces Cadmium pure metal on PMMA support. [a] Image acquired with Silver 0.102mm; [b] Image with Cadmium filter 129mm; [c] Image with Indium 147mm.

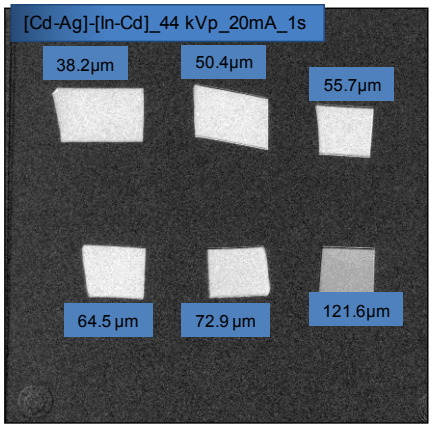

Figure 5.21: KES image of Cadmium 6pieces test phantom.

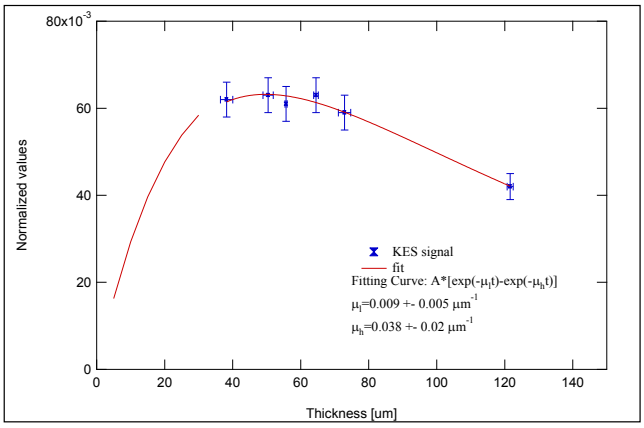

Thickness (μm)	KES signal (GI)	Thic_est (μm)	KES signal_est (net counts)
38.2 ± 1.8	0.062 ± 0.004	5	0.016288
50.4 ± 1.5	0.063 ± 0.004	10	0.029313
55.7 ± 0.3	0.061 ± 0.004	15	0.039617
64.5 ± 0.7	0.063 ± 0.004	20	0.047655
72.9 ± 1.8	0.059 ± 0.004	25	0.05381
121.6 ± 0.9	0.042 ± 0.003	30	0.058404

Figure 5.22: (left) Plot of KES signal versus thicknesses of Cd pure metal foils. (right) Results tabulated for each strip.

By analysing the experimental results obtained by KES technique, gives us possible information for the response of this technique against different quantity of element of interest.By fitting data the function presented in graph (5.22 left) , it is justified from theoretical assumptions for the linear subtraction technique. (Refer to chapter 1, eq 1.17)

The linear attenuated coefficient of cadmium element estimated form fit are: $\mu_L = (0.009 \pm 0.005)\mu m^{-1}$ ([Cd-Ag] E_L=26.1keV) and $\mu_L = (0.038 \pm 0.02)\mu m^{-1}$ ([In -Ag] E_H=27.3keV) While theoretically they are $\mu_H = 0.041\mu m^{-1}$ $\mu_L = 0.008\mu m^{-1}$, that means are in a good agreement. From results, KES technique using balanced filters has a good linearity in detection of cadmium pure element in a range from few microns to 35 μm. (by using a W tube with a tuneable energy 49 kVp and radeye200 CMOS as detector)

Also to determine the repeatability of measurements using the KES technique the experiment it is repeated on the same sample for observing the repeatability of technique. Results are repeatable and with an error not more than 5 %, Fig 5.23.

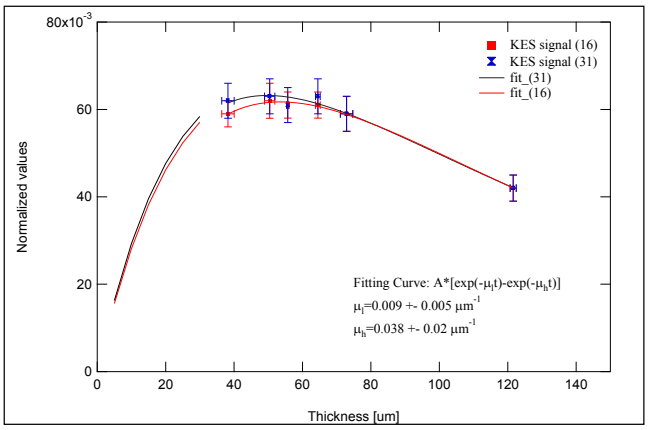

Thickness (μm)	KES signal (exp_31)	KES signal (exp_16)
38.2 ± 1.8	0.062 ± 0.004	0.059 ± 0.003
50.4 ± 1.5	0.063 ± 0.004	0.062 ± 0.004
55.7 ± 0.3	0.061 ± 0.004	0.061 ± 0.003
64.5 ± 0.7	0.063 ± 0.004	0.061 ± 0.003
72.9 ± 1.8	0.059 ± 0.004	0.059 ± 0.004
121.6 ± 0.9	0.042 ± 0.003	0.042 ± 0.003

Figure 5.23: Plot of KES signal for two experiments indicated by blue and red markers and tabulated results.

5.6 Test Painting

K-edge subtraction technique to investigate cadmium distribution has been also applied to a oil painting in cardboard support. Results will be shown in following.

5.6.1 ”Lungo a strada per Rimini” from Pazzini

Radiography using balanced filters has been performed on a small oil painting on cardboard, ”Lungo a strada per Rimini” (Fig. 5.3[a]), a painting from Pazzini.

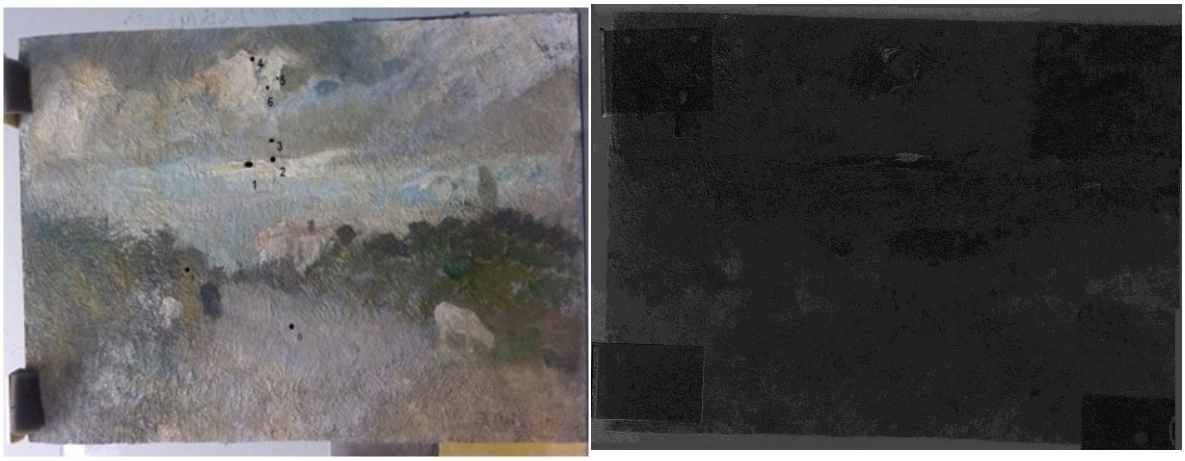

[a] [b]

Figure 5.24: [a] “Lungo a strada per Rimini” painting, [b] imaging by LA

The whole painting surface (about 21×32cm) has been scanned by a fixed remote Radeye200 detector.

A preliminary XRF analysis of painting has been performed to confirm the presence of Cadmium, as presented in (Fig.5.24 [a]). Measurements are performed with the same energies, KVp and current settings of other Cadmium analysis. The cadmium distribution it is shown in Fig.5.24 [b].

There is presence of Cd on points preliminary detected and also some other are on the right down corner of paint.

CHAPTER 6

6. X-ray fluorescence analysis

In order to validate the k-edge filter subtraction technique for cadmium element with the same samples complementary analyses are preformed with micro X-ray fluorescence spectrometry (XRF). In this chapter theoretical aspects about the XRF, characterization of XRF system used in terms of principal of work, sampling area of detection system, will be described.

6.1 Theoretical aspects of X-ray fluorescence and artefacts

The X-ray fluorescence (XRF) spectrometry is a well-established method of quantitative element analysis, which is based on the ionization of the atoms of the material being investigated by an energetic beam of primary X-rays.

The characteristic radiation that is emitted by the ionized atoms upon relaxation (100fs) contains information on the nature and the abundance of the elemental constituents present. The measured spectrum is a line spectrum with all characteristic lines superimposed above a certain fluctuating background, which is caused by other interaction processes, mainly the elastic and inelastic scattering of the primary radiation on sample and substrate.

In practice supposing that the surface area of object is too large comparing the area illuminated by incident x-ray beam, the characteristic photons of an element dI_f the will be emitted in the direction of detector, indicated from angle Ψ (like in Fig.6.1), when the incident x rays hit the surface of the sample in an angle φ the data are:

$$dI_f = I_0(E)\varepsilon_g\varepsilon_r\omega_f F_f p_f \tau_f(E) w_f e^{-\mu(E)\rho\frac{x}{\cos(\varphi)}} e^{-\mu(E_f)\rho\frac{x}{\cos(\Psi)}} dx \qquad (6.1)$$

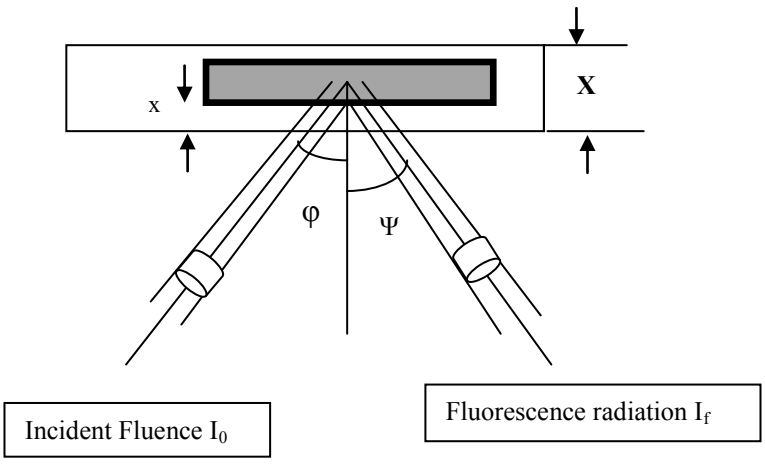

Figure 6.1: The diagram of the production of the phenomenon of x-ray fluorescence.

where: $I_0(E)$ is fluence of incident beam (photons/smm^2), ε_g geometric efficiency of the system (connected with distance between detector source and sample), ε_r the efficiency for detection of characteristic photons, ω_f yield of fluorescence, F_f is the fraction of photoelectric interaction that is possible to generate characteristic photons of energy E_f, p_f is the probability of emissions of photons with an energy E_f following a primary interaction, $\tau_f(E)$ is the partial mass absorption coefficient for photoelectric effect, w_f is the weight fraction of the element and ρ is the density of sample. With two exponential terms it's possible to estimate how many photons of the primary beam goes on the element in the surface with interest and how many photons are emitted from area of sample, $\mu(E)$ e $\mu(E_f)$ there are mass attenuation coefficients (cm^2/g) of sample in the energies respectively of primary radiation and characteristic photons.

Integrate in all thickness of sample the relation gives the dependence of number of photons that emerge from surface in an material complete uniform:

$$I_f = I_0(E)\varepsilon_g\varepsilon_r\omega_f F_f p_f \tau_f(E) w_f \frac{1 - e^{-(\frac{\mu(E_f)}{\cos(\Psi)} + \frac{\mu(E)}{\cos(\varphi)})\rho x}}{\frac{\mu(E_f)}{\cos(\Psi)} + \frac{\mu(E)}{\cos(\varphi)}} \qquad (6.2)$$

The independence from the characteristics of area where it is emitted the fluorescence it is a problem that might be avoided by irradiate by narrow x-ray beams that reduce surface exanimate and allow in this way a hit in a flat surface. So in many cases the dependence in angels it is not take into account and the relation will be simplified:

$$I_f = I_0(E)\varepsilon_g\varepsilon_r\omega_f F_f p_f \tau_f(E) w_a \frac{1 - e^{-(\mu(E_f)+\mu(E))\rho x}}{\mu(E_f) + \mu(E)} \qquad (6.3)$$

$$I_f = k I_0(E) A w_f \rho x_e \qquad (6.4)$$

In the last pass (Eq 6.4) k is a constant dependent on the system and laboratory used, in A are grouped all terms that are dependent only from exited energy and from the element under investigation, x_e that defines the effective thickness that substitute the function of self-absorption. Explicit the self-absorption function it comes discussion on the concrete significant of the effective thickness x_e

$$\rho x_e = \frac{1-e^{-(\mu(E_f)+\mu(E))\rho x}}{\mu(E_f)+\mu(E)} \tag{6.5}$$

Exist the maximum thickness in which x_e can achieve, given by:

$$\rho x_{max} = \frac{1}{\mu(E_f) + \mu(E)} \tag{6.6}$$

Introducing two other thickness that corresponds to the mean free path of photons regarding to primary beam ($\rho x_0 = 1/\mu(E)$) and fluorescence (($\rho x_f = 1/\mu(E_f)$), easy we can show that $x_f /2 < x_{max} \leq x_f$, so the thickness examinated it is determined mainly from the penetration of secondary photons, the fluorescence. Measurements in under surface (layers) or in volumetric are more complex when as exited source is a polychromatic source. In this case we can considering

$$I_f = k\, \varepsilon_g \varepsilon_r \omega_f F_f p_f\, \rho w_f \int_{Es}^{Emax} I_0(E)\, \tau_a(E) x_e(E) dE \tag{6.7}$$

Where the interval of integration are from the threshold of absorption of the element under investigation (E_{abs}) and superior limits it is maximum energy of exited source [29].

Recently the μ-XRF instrumental have been used. The μ-XRF spectroscopy using energy dispersive detectors (EDXRF) is based on the localized excitation and analysis of a small area on the surface of a larger sample, providing information on the lateral distribution of elements present in the material under study. Essentially, a beam of primary X-rays with small cross-section irradiates the sample and induces the emission of fluorescent X-rays from a micro-spot. A suitable detector system collects the fluorescent radiation that carries information on the local composition of the sample, as are silicon drift detectors (Figure 6.2).

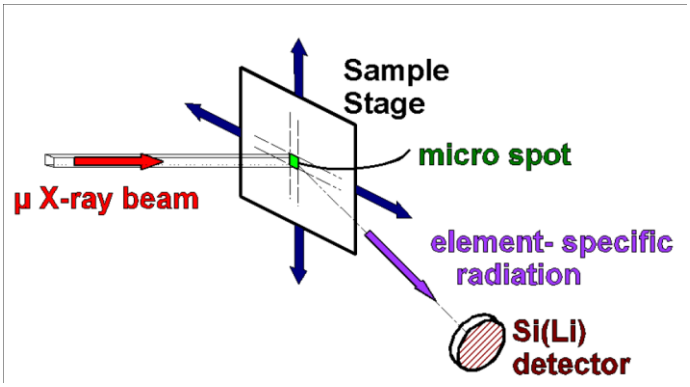

Figure 6.2: Principle of μ-XRF.

While performing analysis with XRF spectroscopy, three main factors contribute to the analytical spectrum: phenomena in the sample, interactions in the detector and the interference with the instrumentation.

The interaction of X-ray source incident with the sample generates several characteristic features in an XRF spectrum which includes: a) *Bremsstrahlung* (continuum / backscatter spectra); b*) Rayleigh peaks* (elastic scattering from sample); c) *Compton peaks* (inelastic scattering).

Bremsstrahlung is a very broad peak due to backscattering of X-rays from sample to detector that may appear in all XRF spectra. Maximum energy of this peak limited by kV applied to X-Ray tube. It is more noticeable in XRF spectra of less dense samples which scatter more of X-ray source photons back to the detector.

Rayleigh peaks arising from target anode in X-ray tube source that may appear in all XRF spectra acquired on that instrument. The peaks show up at characteristic X-ray energies of target because the energy is conserved in this process. In general are observed in spectra of dense samples as weak peaks (due to increased absorption of X-ray source photons by sample).

Compton peaks are inelastic scattering energy peaks arising from target element in X- ray tube and will be present in all XRF spectra acquired on that instrument. Because of non conservation of the energy (some energy is lost in this process) peaks show up at energies slightly less than characteristic X-ray tube target energies. Typically observed in spectra of low density samples as fairly intense peaks (these peaks are wider than Rayleigh peaks).

All mentioned spectra are present by XRF diagram acquired by ArtaxBruker200 system, with primary Mo X-ray source for a Plexiglas sample and Plexiglas + cooper wire. (maximum 50 kV peak voltage).

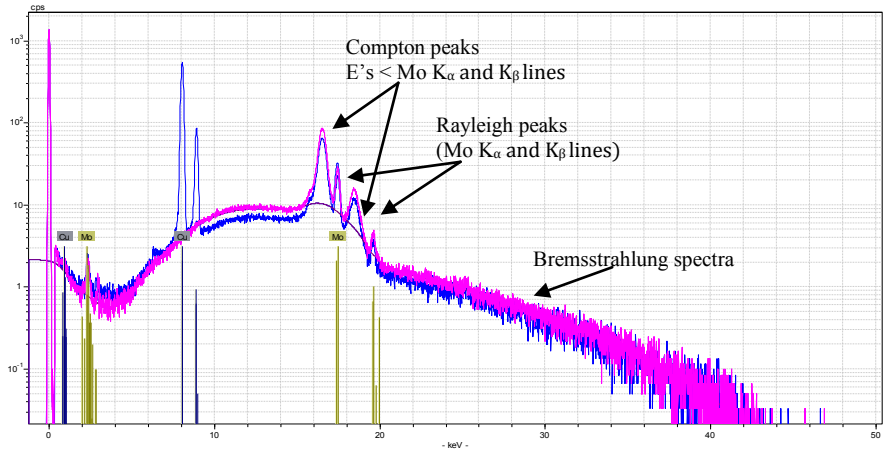

Figure 6.3: XRF spectra in semi log scale counts per second versus energy in keV. Red spectrum from a Plexiglas sample. Blue one spectrum form Plexiglas + copper wire.

Due to interactions of X-ray fluorescence photons from the sample *in the detector* two main artefacts will be generated: sum peaks and escape peaks. The *sum peaks* are due to the arrival of 2 photons at the detector at the same time (i.e., $K_\alpha+K_\alpha$, $K_\alpha+K_\beta$) and are more noticeable in XRF spectra that have high concentrations of an element. *Escape peaks* comes due to the absorption of some of the energy of a photon by Si atoms in the detector ($E_{Observed} = E_{Incident} - E_{Si}$ where $E_{Si} = 1.74$ keV). It is encountered more in XRF spectra that have high concentrations of an element and for lower Z elements. In both cases these artefacts can be reduced by keeping count rates low. And about the *interference with the instrumentation* false peaks may be arise due to contaminations in container of samples or trace levels of elements contaminated window or detector materials in XRF [29][30].

6.2 Characterization of μXRF system

Measurements for the presence of the cadmium element are performed with μXRF system ArtaxBruker200, installed at Larix laboratory at Department of Physics, University of Ferrara.

The system has an excitement X- ray source of Molybdenum target with a focal spot 1.2 x 0.1 mm^2 and a tilted angle 6 degree[1]. The maximum energy achieved is 50kVp and with a current not more than 1000 μA. The X-ray beam could be restricted by a collimator which can vary in a diameter from 200 to 1000 μm, depending on the type of collimator used.

The detector that measures the x-ray characteristics emitted by sample is Silicon Drift detector XFLASH 3001 with a resolution less than 150eV. It has an area of 10 mm^2 and is a SDD Peltier cooled detector.

For validate our technique k-edge subtraction imaging by using balanced filters in evaluation of cadmium element, XRF measurements are performed on the same sample and the same position for the red cadmium on canvas.

To obtain optimal correlation between KES and XRF measurements for the sampling area of the SDD has been performed and will be presented below.

[1] Artax UserManual

6.2.1 Principal work of Artax Bruker200

A schematic of μXRF spectrometer Artax200 is illustrated in Fig. 6.4[a]. Main components are the tripod, measurement head, xyz adjustment, electronics unit, terminal and the computer data receiver (in order with the numbers labelled).

A main factor that needed to be stressed is the principle of optical triangulation that is is used for the adjustment of the working distance between sample and measuring head illustrated by Fig. 6.4 [b]. The excitation beam and optical axis of the detector must meet at the measuring point of the sample precisely when, in the video image, the cross-hairs meet the laser spot at the same measuring point of the sample, otherwise underestimated or overestimated results will be obtained (Fig. 6.4[c]. The components of measuring head in correspondence with labelling numbers, shown by Fig. 6.4 [b] are the sample, X-ray excitation beam, X-ray fluorescence and scattered radiation, radiation registered by detector, CCD camera, sample lighting, laser pointer for positioning and collision sensor

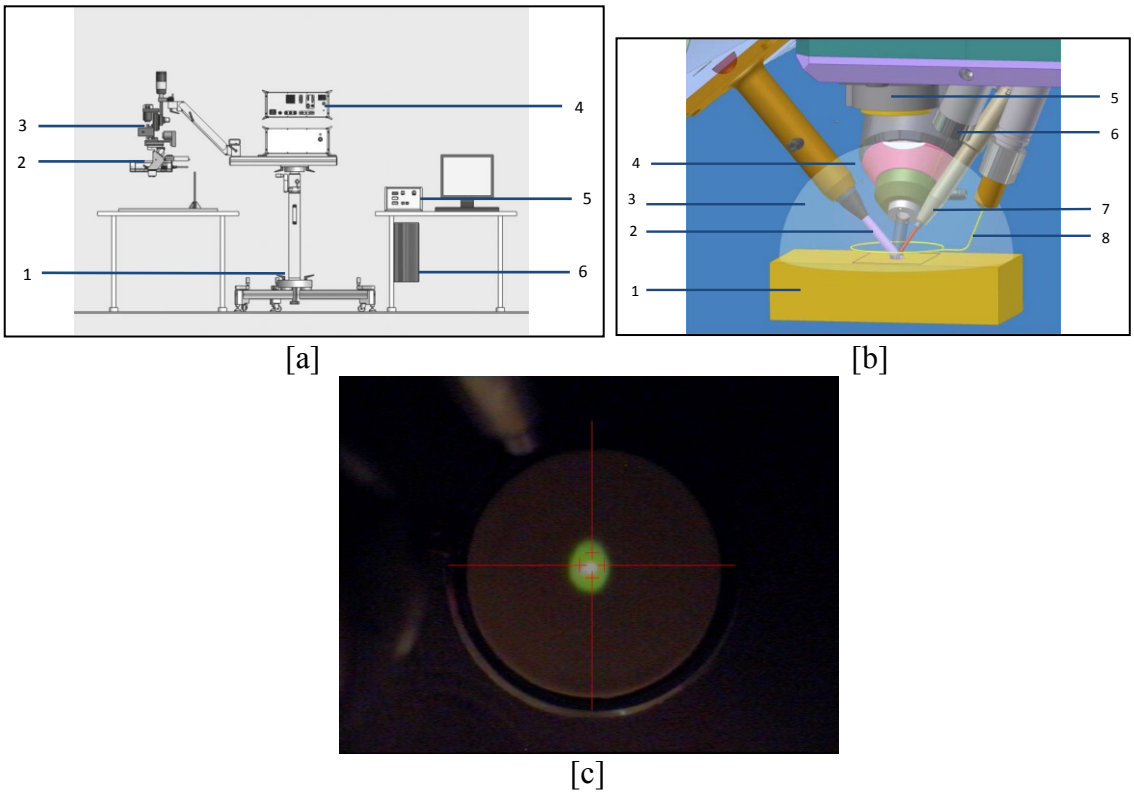

Figure 6.4: [a] Schematic of ARTAX unit [b] Measuring head scheme, [c] CCD camera image on bronze standard with an x-ray beam collimated by 1 mm collimator.

A semiconductor silicon drift detector it is used for the detection of X-ray fluorescence radiation from the sample. It works according to the drift chamber principle (SDD). Detector receives the characteristic X-ray radiation and converts it into current pulses

which are amplified and digitised in the pre-amplifier and XSPV. A cross section of SDD and the operation mode are shown in the Fig. 6.5[a] and [b].

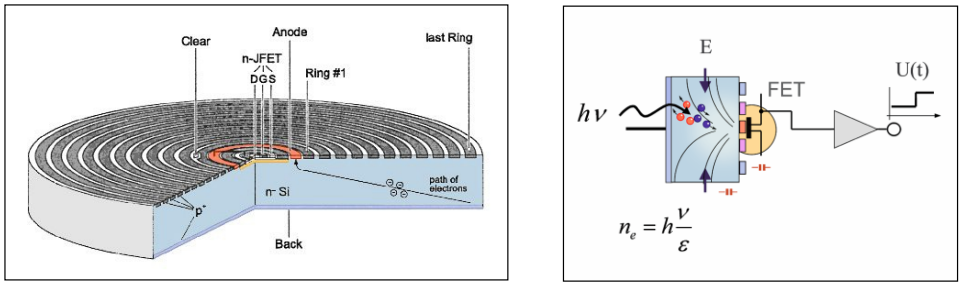

[a] [b]

Figure 6.5: [a] Cross-section through an SDD X-ray detector, [b] Mode of operation of an SDD-X-ray detector

The digital output signals are processed further by the XDSP digital signal processor, combined into complete spectra and passed on to the measurement computer and processed by the ARTAX™ Software. The semi-conductor detector is cooled electro-thermically to minimize noise.

6.2.2 Measurements of sampling area

In order to determine the sampling area of SDD detector a Copper (Cu) wire was scanned at different positions along the beam axis. This measurement also yields information about the sensitivity of spatial resolution of the system to slight changes in position along the beam axis.

Measurements are performed for a setup of the excitement source (Mo) at 50 kVp with a current 700 ?A and for a time period of 60s. Also a collimator of 1 mm in diameter was used in front of excitation x- ray beam. The copper wire used was with a diameter of 50 µm.

Before starting the measurements is checked for the alignment of optical axis of triangle source-detector-CCD camera with a phosphor plate and calibration channel–energy it is performed with standard of bronze material. The copper wire it is stacked in a Plexiglas plate and fixed over linear translation stage, which make possible the movements of the sample in vertical and horizontal directions against the head of measurement, shown in the Fig.6.6.

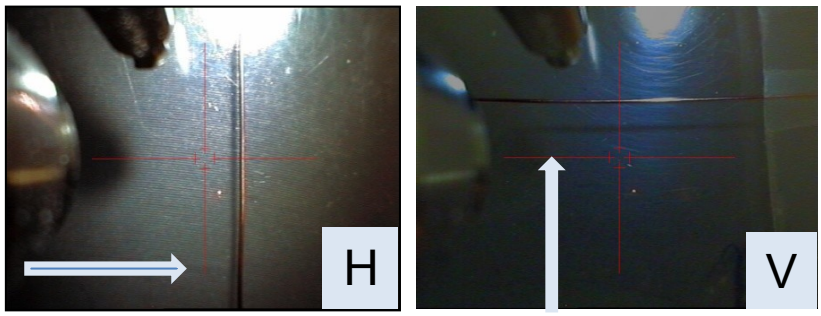

Figure 6.6: Photo by the CCD camera of copper wire positioning against the head measurements.

Data are sampled for a distance approximately ± 2000 μm along X-ray beam axis and a step 100 μm. Using the Cu Kα fluorescence line, the net counts of copper content (normalized net counts) are graphed as a function of the distance.

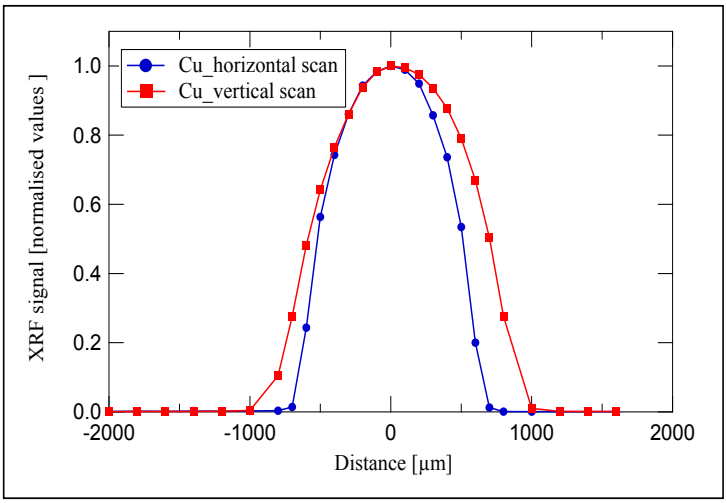

Figure 6.7: Measured scan profile from a line scan across a 50μm Cu wire for the Kα line.

The sampling area is determined by fitting data with two possible functions, Gaussian and elliptical with parameters tabulated on the Tab 6.1 and Tab 6.2

Table 6.1: Parameters for Gaussian fit for scan profiles of 50μm Cu wire.

	Horizontal scan profile	Vertical scan profile
FWHM	747.4 μm [7.7 pixel]	940.7μm [9.7 pixel]
Sigma	318.0 μm	400.3 μm

Table 6.2: Parameters for elliptical fit for scan profiles of 50μm Cu wire.

Elliptical	H. scan profile	V. scan profile
Radius	A=743 ±7μm	B=614 ±2μm

Based on these results a matrix as a product of 2 functions that present the vertical and horizontal scan profile of Cu wire will be produced. The dimensions of the matrix will be defined based on the three sigma of Gaussian profile function matrix in data that are defined by the parameter of FWHM for the Gaussian profile [suggested by literature]. The matrix converted in an image and presented in figure below.

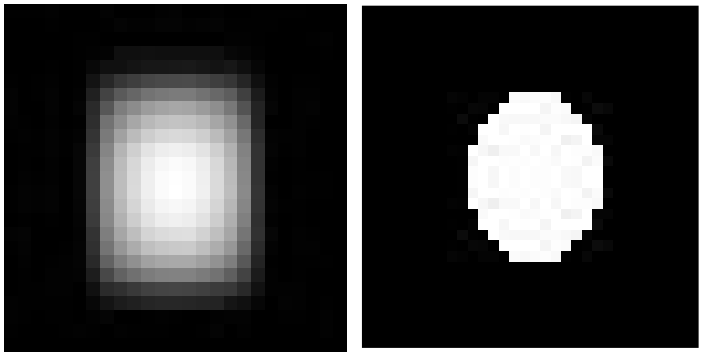

Figure 6.8: Image matrix as product of point spread function of XRF system in vertical and horizontal direction. (Gaussian left and elliptical left)

The matrix (presents the point spread function of the SSD detector) will be convolved with images obtained by the *k*-edge imaging technique for the same sample. After convolution comparison of results from two techniques will be done and a possible correlation between them will be estimated.

6.3 Measurements of cadmium element with XRF

For validating the KES technique with XRF measurements are performed with the same samples. XRF measurements have been obtained at 50 kVp, with a current 700μA and for a period time of 60s. Results based on net counts on Kα line of the cadmium element will be presented.

6.3.1 Red cadmium 5sections

Measurements with μXRF system (Artax Bruker200) have been done in point scan modality. After alignment of the sample with the head of unit, measurements are

performed over canvas test starting at labelled point along all 5 sections. The step of each point measured was 1.3 mm, distance dictated form base profile of Cu wire scan in horizontal direction.

Spectra are processed by Artax software (Fig 6.9 [a]) and the net counts of cadmium content in each point scan are presented on Fig 6.9 [b]. Also the average values of each section in canvas test sample are presented in Fig 6.10.

According the results the 5 section cadmium red it was not like it was expected in increasing order thought the sections (1 to 5). The first one has a lower concentration the second and the third one are quasi the same and the fifth section is in higher concentration.

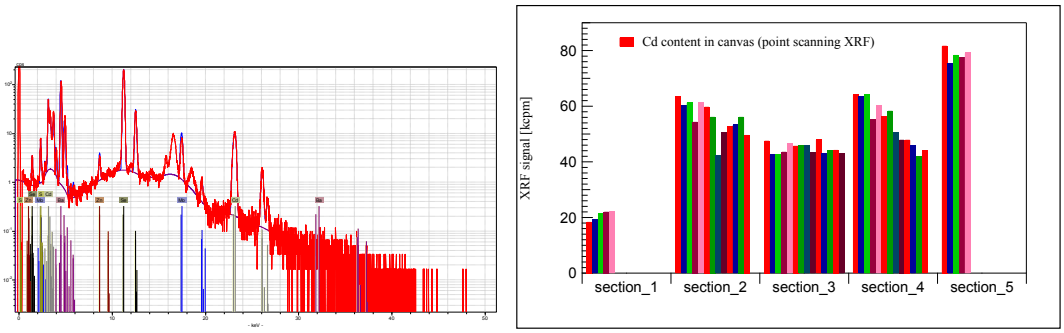

[a] [b]

Figure 6.9: [a] XRF spectrum of red cadmium sample, [b] Cadmium content for each point scanned by XRF.

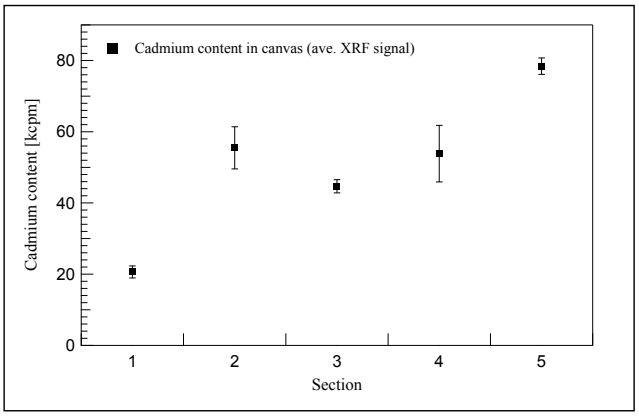

	XRF_average [kcpm]
RedCd_sect_1	20.6 ± 1.7
RedCd_sect_2	55.5 ± 5.9
RedCd_sect_3	44.7 ± 1.9
RedCd_sect_4	53.8 ± 7.9
RedCd_sect_5	78.4 ± 2.3

Figure 6.10: Average Cadmium content for each section. (Graphically presented (left) and tabulated data (right).

6.3.2 Four strips

Measurements with μXRF system (Artax Bruker200) have been done in the same condition as previous sample. In this case it is performed only one measurement for each

strip nearly to the centre part. Net counts of cadmium content are presented by table Table 6.3:

Table 6.3: Cadmium net counts for 4 strips red cadmium sample.

4_strips_ Cd_red_pigment	Cd_Netcounts (cpm)
1	122706± 356
2	190098± 442
3	216005± 471
4	219621± 476

6.3.3 Yellow Naples and Cadmium red

On the sample three points are scanned and tabulated on the table Tab. 6.4.

Table 6.4: Cadmium net counts for Yellow Naples and red Cadmium sample.

Test layers	Cd_Netcounts (cpm)
Y_N ($Pb_2Sb_2O_7$)	1993 ± 44.6
Cd_red (CdS +CdSe)+GN	38542 ± 196
Cadmium red	34115 ± 185

6.3.4 Cadmium 6pieces

Measurements are performed for the same setup of mo x ray source with 50kVp and current 700μA.

Table 6.5: Cadmium net counts for 6pieces of Cd pure element.

Thickness (μm)	Cd_ Net counts (cpm)
38.2 ± 1.8	313032 ± 568
50.4 ± 1.5	340420 ± 591
55.7 ± 0.3	351507 ± 600
64.5 ± 0.7	363352 ± 610
72.9 ± 1.8	371435 ± 616
121.6 ± 0.9	389208 ± 630

6.3.5 Pazzini painting

For Pazzini paint are performed some measurement in parts were cadmium presence was preliminary traced by UV method. Results for net counts of Cadmium content are presented in the table below for the region indicated on the painting, the Fig_6.11. Netcounts for Cd Kα fluorescence line are tabulated on the table Tab. 6.6, in correspondence with labelling.

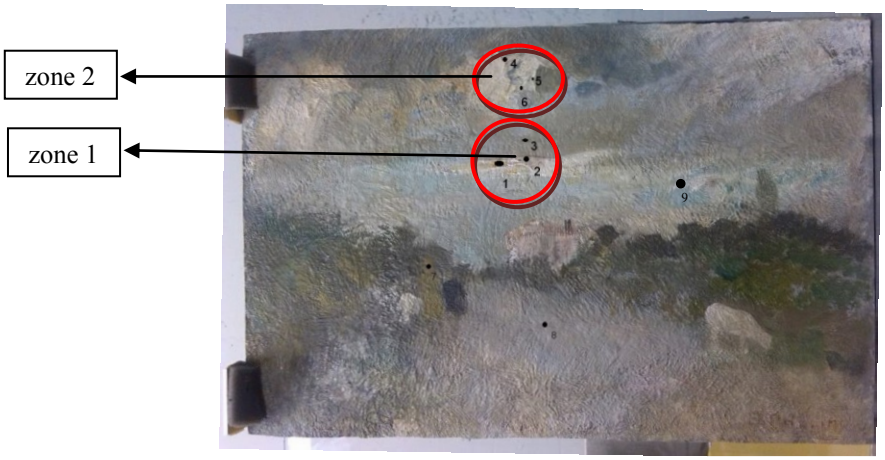

Figure 6.11: Pazzini paint labelled at points scanned by XRF.

Table 6.6: Cadmium net counts Pazzini paint

Painting scanned area	Net_counts_Cd [cpm]
1_zone_1	18462 ± 142
2_zone_ 1	6049 ± 88
3_zone_1	3013 ± 70
4_zone_2	4941 ± 80
5_zone_2	6946 ± 95
6_zone_2	5146 ± 81
7_women head	21504 ± 155
8_grey zone	1299 ± 57
9_ azurite	3873 ± 76

CHAPTER 7

Correlation between KES and XRF technique for estimation of cadmium content in paintings.

In this chapter it will be discussed the results carry out from KES technique and XRF measurements. For validation of technique and possible quantitative measurements comparison for estimated values of cadmium content will be reported and a correlation between them will be done mainly for test sample cadmium red 5sections in canvas.

7.1 Selection of ROI in images obtained by KES technique

For comparison between the KES and XRF technique the selection of region of interest on image it is done based on data of sampling area of XRF system.

Two ways are used for selection of ROI:

1. Selecting an elliptical area of 0.59 mm^2 in image without convolution with PSF of XRF
2. Point selection on image convolved with PSF of sampling area of XRF (Gaussian and elliptical)

Selecting an elliptical area direct on final KES image it is dictated by the full width at half maximum of Gaussian fit of sampling area of XRF system.

7.2 Correlation between KES and XRF signal for 5sections Cadmium red sample test

The average values for cadmium content estimated by KES technique and XRF spectrometry on 5section Cd red sample, are presented graphically as averaged cadmium net content in each section (form 1 to 5), the Fig. 7.1. It is visible that both techniques response to cadmium presence linearly and shows that cadmium content for each section of canvas test.

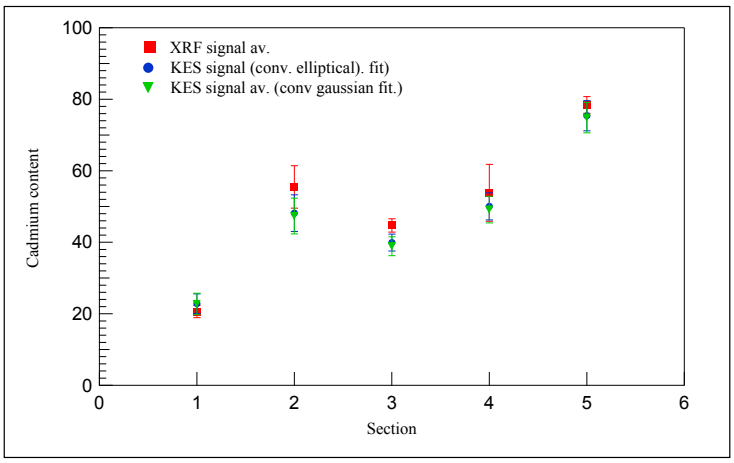

Figure 7.1: Cd average values of each section of Cadmium red 5sections canvas test.

For studying the correlation between the measurements of cadmium element measured by KES technique with the results obtained from XRF, a comparison of their data has been done and by using a linear fit correlation factors are determined (resumed in table 7.6.)
Three cases are studying for finding the best correlation between KES and XRF technique.

7.2.1 Comparison of KES and XRF results without convolution of images with PSF of XRF

Data from images are extracted by selecting direct an elliptical area of 0.59 mm^2 on it with a step 1.3 mm, and in the same line when the XRF measurements have been performed.
Around 50 data from KES and XRF for Cd_red 5section are graphed as KES signal in function of XRF signal and a linear fit has been done (Fig.7.2 left). Also the averaged data for each section are compared between techniques and are presented by the fig.7.2 right.
The errors bar for KES signal are connected to standard deviation over area selected on images while for XRF technique to the standard deviation of the netcounts values measured to each section.

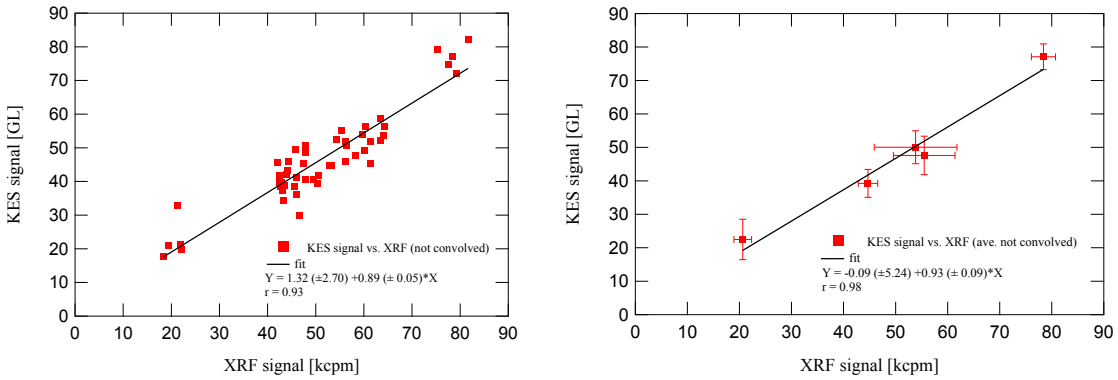

Figure 7.2: The correlation between KES and XRF technique for Cd content on Cd_red5sections when no convolution is applied.

The correlation between KES signal and XRF signal for each data scanned is given by the relationship KESsignal = (1.32 ± 2.70) + (0.89 ± 0.05) XRF_{signal} with a correlation factor r=0.93, and correlation between KES and XRF signal for the averaged data is given by KES_{signal} = (-0.9 ± 5.24) + (0.93 ± 0.09) XRF_{signal} with r=0.98.

Table 7.1: Tabulated results for both techniques KES and XRF for cadmium content in the Cd red 5 section sample.

Cdred canvas test	KES mean (no_conv) [Gl]	XRF_average [kcpm]
RedCd_sect_1	22.5 ± 6.02	20.6 ± 1.7
RedCd_sect_2	47.6 ± 5.8	55.49 ± 5.9
RedCd_sect_3	39.3 ± 4.2	44.7 ± 1.9
RedCd_sect_4	50.0 ± 4.9	53.8 ± 7.9
RedCd_sect_5	77.1 ± 3.9	78.4 ± 2.3

7.2.2 Comparison of KES and XRF results, convolution with PSF from G. fit

After making convolution of final image obtained by KES technique the selection ROI in image have been done as a point selection, because it is supposed that after this "filtering" the two detectors sample the same signal on the same sample. Simple diagram for steps used for elaborating the image is shown in Fig. 7.3.

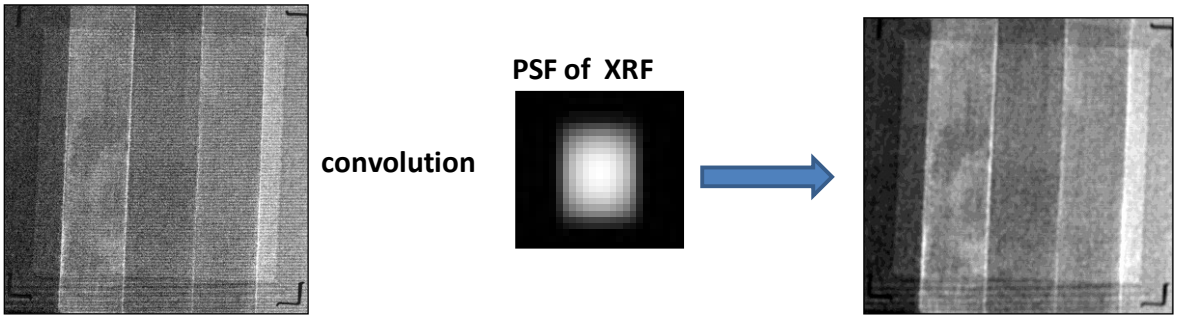

Figure 7.3: Cadmium distributed image, PSF of XRF signal (G.f), final image after convolution.

In the same way, results for cadmium content from both techniques KES signal (on images) and XRF signal (net counts by fluorescence Cd Kα line) are compared and built graphically.

Both cases are studied, correlation for each point scanned on sample and the average values of points in one section (each section is with the same number of Cd red pigment layers), presented in Fig. 7.4. From a linear fit, a correlation between KES and XRF technique it is determined.

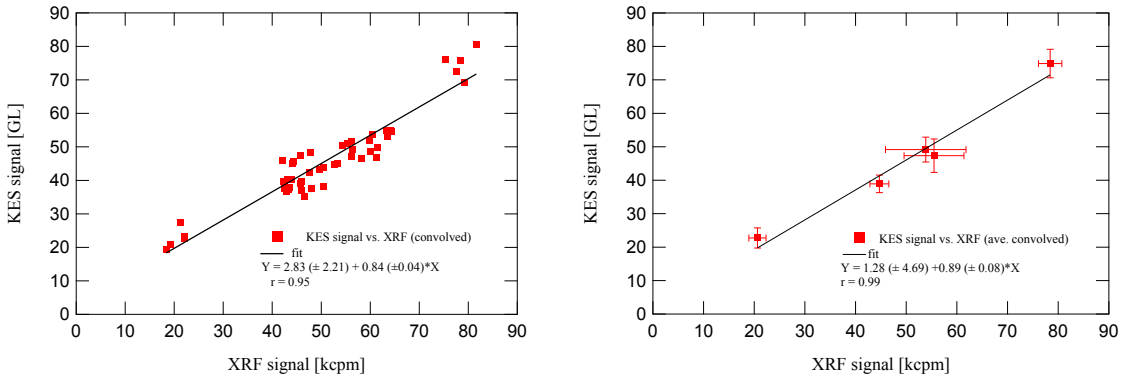

Figure 7.4: The correlation between KES and XRF technique for Cd content on Cd_red5sections when convolution is applied (Gaussian fit).

Correlation between KES signal and XRF for 50 data is given by the relationship $KES_{signal}=(2.83 \pm 2.21) + 0.84 \pm 0.04)XRF_{signal}$ with a correlation factor r=0.95, and for averaged data in the same section is given by relationship $KES_{signal}=(1.28 \pm 4.69) + (0.89 \pm 0.08)XRF_{signal}$ with r = 0.99.

Table 7.2: Cadmium content estimated on KES (convoked with PSF of XRF signal, G.F) and average XRF signal.

Cd_red canvas test	KES mean convolved (G.fit) [Gl]	XRF_average [kcpm]
RedCd_sect_1	22.7 ± 3.0	20.6 ± 1.7
RedCd_sect_2	47.3 ± 5.0	55.5 ± 5.9
RedCd_sect_3	38.9 ± 2.6	44.7 ± 1.9
RedCd_sect_4	49.2 ± 3.7	53.8 ± 7.9
RedCd_sect_5	74.9 ± 4.3	78.4 ± 2.3

7.2.3 Comparison of KES and XRF results, convolution with PSF from elliptical fit

By convolving the image with elliptical point spread function the procedure is repeated (fig 7.5). Are extracted the data by point selection in the image along on the scan line in which the XRF measurements have been performed.

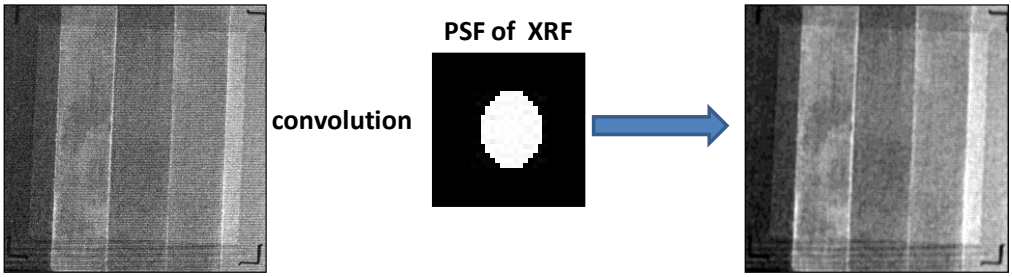

Figure 7.5: Cadmium distributed image, PSF of XRF signal (G.f), final image after convolution.

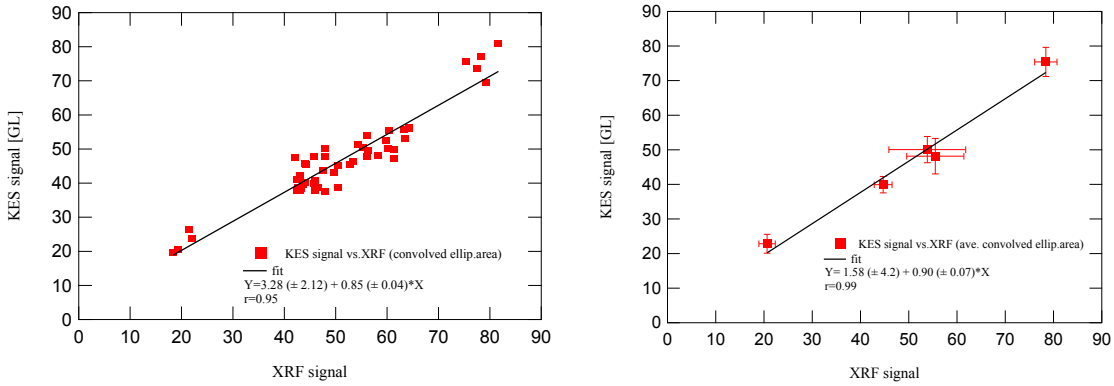

Figure 7.6: The correlation between KES and XRF technique for Cadmium content on Cd_red 5sections test when convolution is applied (elliptical fit).

Correlation between KES signal and XRF for 50 data is given by the relationship $KES_{signal}=(3.28 \pm 2.12) + (0.85 \pm 0.04)XRF_{signal}$ with a correlation factor r=0.95, and for averaged data in the same section is given by relationship $KES_{signal}=(1.58 \pm 4.20) + (0.9 \pm 0.07)XRF_{signal}$ with r = 0.99.

Table 7.3: Cadmium content estimated on KES (convolved with PSF of XRF signal, Ellip.F) and average XRF signal.

Cdred canvas test	KES mean convolved_(Ell.fit) [Gl]	XRF_average [kcpm]
RedCd_sect_1	22.8 ± 2.7	20.6 ± 1.7
RedCd_sect_2	48.1 ± 5.1	55.9 ± 5.9
RedCd_sect_3	39.9 ± 2.4	44.7 ± 1.9
RedCd_sect_4	50.1 ± 3.8	53.9 ± 7.9
RedCd_sect_5	75.4 ± 4.2	78.4 ± 2.3

The parameters of correlation between KES and XRF technique are summarised on the table below. The linear regression fir used it was of Y= B*X + A.

Table 7.4: The correlation parameters obtained for KES measurements and XRF measurements. KES = B*XRF + A

Cd_red canvas test	$B \pm \sigma_B$	$A \pm \sigma_A$	Correlation Factor r
KES vs. XRF signal direct in image (index:1_50 data)	0.89 ± 0.05	1.32 ± 2.70	r1=0.93
(index:2_5 averaged data)	0.93 ± 0.09	-0.09 ± 5.24	r2=0.98
KES vs. XRF signal (convolved G.fit)	0.84 ± 0.04	2.83 ± 2.21	r1=0.95
	0.89 ± 0.08	1.28 ± 4.69	r2=0.99
KES vs. XRF signal (convolved Ell. fit)	0.85 ± 0.04	3.28 ± 2.12	r1=0.95
	0.90 ± 0.07	1.58 ± 4.2	r2=0.99

From these results it can be seen that there is good correlation between KES signal and XRF signal. In particular, the linear correlation factor r obtained for averaged values in the same section are more closed to unity. While, the linear regression coefficient obtained for point by point data is relatively good, which means selection of an area is better in digital images than a point selection over images.

7.3 Correlation between mass density (L.A signal) and XRF measurements

For a possible correlation between the mass density of cadmium content in canvas test and XRF netcounts will be presented. Images of three filters Ag, Cd and In have been processed by L.A by using a plug-in in ImageJ program. Three cases will be considered when the selection of region of interest will be **a)** direct in image processed by L.A **b)** in processed by L.A and after convolved by Gaussian PSF **c)** after convolution with elliptical PSF with image convolved in the same conditions as in KES subtraction. The data are presented graphically as L.A signals vs. XRF net counts of cadmium content and a summarise of results is presented in Table 7.5. From results there is a good correlation.

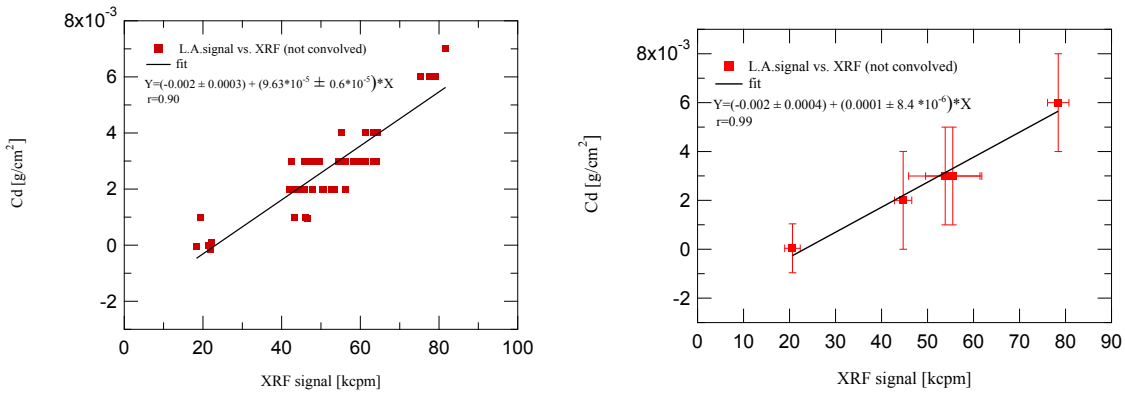

Figure7.7: The correlation between L.A results and XRF technique for Cd content on Cd_red5sections when no convolution is applied.

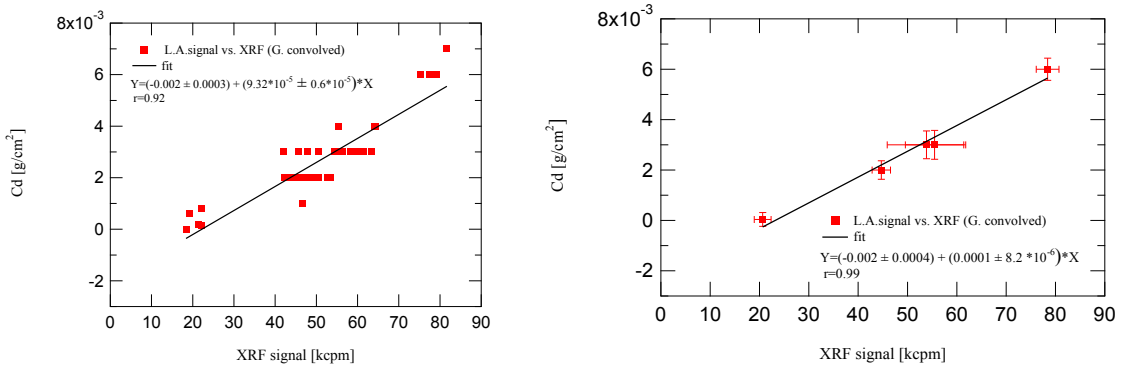

Figure7.8: The correlation between L.A results and XRF technique for Cd content on Cd_red5sections when convolution is applied (Gaussian fit).

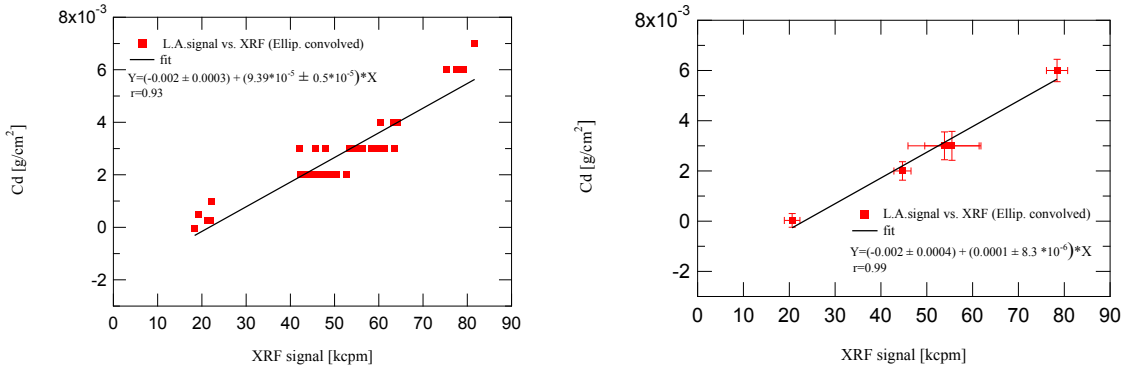

Figure7.9: The correlation between L.A results and XRF technique for Cd content on Cd_red5sections when convolution is applied (elliptical fit).

Table 7.5: The correlation parameters obtained for L.A applied in images and XRF measurements. L.A signal = B*XRF + A

Cd_red canvas test	$B \pm \sigma_B$	$A \pm \sigma_A$	Correlation Factor r
L.A vs. XRF signal direct in image (index:1_50 data) (index:2_5 averaged data)	$9.6*10^{-5} \pm 0.6*10^{-5}$	$-2*10^{-3} \pm 0.3*10^{-3}$	r1=0.90
	$1*10^{-4} \pm 0.08*10^{-4}$	$-2*10^{-3} \pm 0.4*10^{-3}$	r2=0.99
L.A vs. XRF signal (convolved G.fit)	$9.3*10^{-5} \pm 0.6*10^{-5}$	$-2*10^{-3} \pm 0.3*10^{-3}$	r1=0.92
	$1*10^{-4} \pm 0.8*10^{-5}$	$-2*10^{-3} \pm 0.4*10^{-3}$	r2=0.99
L.A vs. XRF signal (convolved Ell. fit)	$9.4*10^{-5} \pm 0.5*10^{-5}$	$-2*10^{-3} \pm 0.3*10^{-3}$	r1=0.93
	$1*10^{-4} \pm 0.8*10^{-5}$	$-2*10^{-3} \pm 0.4*10^{-3}$	r2=0.99

Conclusions

In this work application of K-edge subtraction technique using balanced filters for elemental mapping in art paintings has been described and investigated. Theoretical considerations and experimental validation for the technique has been done for the Cadmium element in its pigments and as a pure element.

Furthermore the technique has been compared with the X-ray fluorescence spectrometry for estimation of cadmium content in the same samples.

After a brief overview of the KES technique and XRF regarding to their principal work and expected theoretical considerations a detailed experimental procedure has been made.

The k-edge digital subtraction technique actually is investigated for estimation of cadmium element. By choosing the silver cadmium and indium as filter materials with properly thickness and with k-edge energies very close to the cadmium element, KES technique gives good qualitative and quantitative results. The technique is tested by using remote RadEye200 CMOS sensor.

Analysing different test samples for testing the technique the sensitivity of KES is define considering the linearity response of CMOS detector and sensitivity versus range thicknesses (equivalent of concentration of element in paintings) of element with interest.

From analysis on 5sections Cadmium red test sample which is a canvas test with different layers of red cadmium pigment the sensitivity of KES technique it is studied. The comparison between KES with XRF technique performed for the same sampling area of two detection systems (CMOS sensor with SDD solid state detector) on the same area on the sample shows a very good correlation among them (Table 7.6) The correlation factor is bigger than 0.93.

Table 7.6: Correction factors for KES signal vs. XRF signal.

Cadmium red 5section canvas test	**All data**	**Average data**
KES vs. XRF signal direct in image	(11 ± 5) %	(7 ± 9) %
KES vs .XRF signal (convolved G.fit)	(16 ± 4) %	(11 ± 8) %
KES vs .XRF signal (convolved Ell. fit)	(15 ± 4) %	(10 ± 7) %

The deviation between the correlation coefficients and the unity value quantifies the correction of the KES signal versus XRF, in which it is less than 16 % when point data are selected in images and less than 11 % when an area is selected in KES images.

Also there is a good correlation between L.A signals and XRF results.

Preliminary investigation of technique for cadmium pure element gives a restriction of method in detecting linearly the quantity of element but gives high discrimination of element *present* in a matrix (of orders of micron), which might be possible in using it industry.

Even why in Cd pure element the linearity of the method is limited up to thickness of 35μm, for its pigment thickness according to theoretical simulations corresponds more than 100 μm.

Bibliography

[1] P. Ross. Minutes of the Oakland Meeting. Phys Rev 28, 425, 1926.

[2] S.R Beath and I.A.Cunningham. Pseudo-monoenergitic X-ray diffraction measurements using balanced filters for coherent-scatter computed tomography. Med. Phys. 36, 1839, 2009.

[3] P. Cardarelli, G. Di Domenico, M. Marziani, I. Muçollari, G. Pupillo,F. Sisini, A.Taibi, and M. Gambaccini. Energy distribution measurement of narrow-band ultrashort X-ray beams via k-edge filters subtraction. J App Physics, 112(7):074908, 2012.

[4] B. Jacobson. Dichromatic absorption radiography–dichromography. Acta Radiol. 39: 437–52 1953.

[5] P. Baldelli, L. Bonizzoni, M. Gambaccini, M. Gargano, N. Ludwig, M. Milazzo, L. Pasetti, P. Petrucci, F. Prino, L. Ramello, M. Scotti, Nuovo Cimento 29, 663-672 2006.

[6] K. Krug, J. Dik, M. Den Leeuw, A.Whitson, J. Tortora, P. Coan, C. Nemoz, A. Bravin. Visualization of pigment distributions in paintings using synchrotron K-edge imaging. Appl. Phys. A 83, 247–251 2006.

[7] NIST.Xcom: Photon cross sections database. http://www.nist.gov/pml/data/Xcom/indeX.cfm.

[8] P.P. Dendy and B. Heaton. Physics for radiologists.

[9] J Beutel, H L. Kundel, R. L.VanMetter. Handbook of medical imaging. SPIE, 2000.

[10] A.C. Konstantindis. Evaluation of digital X-ray detectors for medical imaging applications. PhD thesis. London 2011

[11] A.L.C. Kwawn, J.A. Siebert, and J.M. Boone. An improved method for flat-field correction of flat panel X-ray detector. Med.Phys.Vol.33, No.2, February 2006.

[12] Physics on medical X-ray imaging. (edu.lancaster)

[13] L.A. Lehmann, R.E. Alvarez, A. Macovski, W.R. Brody Med. Phys. 8(5), 659 1981.

[14] F. Albertin, A. Franconieri, M. Gambaccini, D. Moro, and S. Chiozzi. A quasi-monochromatic X-ray source for art painting pigments investigations. Appl Phys A 96: (503-510), 2009.

[15] A. Sarnelli, , A. Taibi, A. Tuffanelli, G. Baladzzi, D. Bollini, A. E. Cabal Rodrigues, M. Gombia, F. Prino, L. Ramello, E. Tomassi and M. Gambaccini. K-edge digital subtraction imaging based on a dichromatic and compact X-ray source. Phys. Med. Biol. (49) (3291-3305), 2004.

[16] Pigments through the Ages.

[17] J. P. Gustafson. Soil chemical behaviour of cadmium pigments from paints.

[18] AMPTEK Inc XR-100T-CZT Manual February 2000.

[19] Rad-icon imaging. Remote RadEye X-Ray Camera data sheet.

[20] G. Weckler. "Operation of p-n junction photdetectors in a photon flux integrating mode," IEEE J. Solid-State Circuits, vol. 2, pp. 65–73, Sept. 1967.

[21] A. El Gamal and H. Eltoukhy. An introduction to the technology design and performance limits presenting recent developments and future directions.

[22] Th. Graeve and G. P. Weckler. High-resolution CMOS imaging detector. Rad-icon Imaging corp.

[23] Rad-icon Imaging Corp. Imaging Detector Lifetime and Radiation Damage.

[24] Rad-icon Imaging Corp. DQE Measurements for RadEye EV Sensors.

[25] R. M Nishikawa. The Fundamentals of MTF, Wiener Spectra, and DQE.

[26] I.A. Cunningham, Reid BK. Signal and noise modulation transfer function determinations using slit, wire and edge techniques. Med Phys. 19(4):1037-44, 1992.

[27] P. Kirkpatrick. On the Theory and Use of Ross Filters. Rev. Sci. In strum. 10, 186 1939. (http://dx.doi.org/10.1063/1.1751523)

[28] P. Kirkpatrick. Theory and Use of Ross Filters II. Rev. Sci. In strum. 15, 223 1944. (http://dx.doi.org/10.1063/1.1770273)

[29] G. E. Gigante and S. Ridolfi. La tecnica della Fluorescenza a raggi X.

[30] ARTAX™ USER MANUAL

[31] G. Gauglitz and T. Vo-Dinh. The Handbook of Spectroscopy. Wiley-VCH, ISBN 3-527-29782-0, 1000, 2003.